UNIVERSITÀ DI PISA

DIPARTIMENTO DI FISICA
Corso di Laurea Magistrale in Fisica

Tesi di Laurea Magistrale

Graphene strain engineering using micropatterned SiN membranes

Candidato:
Francesca Fabiana Settembrini

Relatori:
Prof. Alessandro Tredicucci
Prof. Stefano Roddaro

Anno Accademico 2015-2016

Table of contents

1 Introduction **3**

2 Graphene **6**

2.1 Structure and properties 6

2.2 Production of graphene 9

3 Mechanical deformation of graphene **12**

3.1 Introduction to continuum mechanics 12

3.2 Small deformation limit and linear elastic response 13

4 Raman spectroscopy as an analysis tool for graphene **17**

4.1 Raman spectra of mono-layer graphene 19

4.2 Uni-axial and bi-axial strain effects on graphene's Raman spectra . . . 22

4.3 Experimental evidences 24

5 Experimental results: Raman spectroscopy on deformed graphene **28**

5.1 Sample fabrication 28

5.1.1 SiN membranes fabrication 28

5.1.2 Graphene deposition 32

5.2 Description of the Raman setup 36

5.3 Raman spectroscopy on deformed graphene 39

5.3.1 Acquisition mode and parameters 39

5.3.2 Experimental results and interpretation 40

6 Active devices for strain engineering **56**

6.1 Design of SiN membranes with comb actuators 56

6.2 MEMS stretcher 59

7 Conclusion **63**

Bibliography **70**

Introduction

In the last decade, graphene has been the object of great interest in the scientific community because of its peculiar properties, such as high electron mobility, optical transparency and mechanical flexibility [1–3]. These characteristics, along with its two-dimensional nature, make graphene a good candidate for several applications in the context of optoelectronics and opto- and electro-mechanics. These include flexible electronics (touchscreens, rollable e-paper), high-frequency transistors, photodetectors and THz sources [4–6].

The possibility of tailoring graphene electronic properties through the application of suitable strain profiles [7, 8] is especially intriguing and leads to a variety of interesting phenomena: among them, one of the most fascinating options is the possibility to induce a pseudospin-dependent gauge magnetic field, or pseudo magnetic field, when the graphene lattice is subjected to triaxial strain [9, 10]. In this case, moderate deformations of few percent are expected to lead to magnetic fields of various Teslas and to significantly impact the quantum states of electrons in graphene. In the near future, this may lead to the implementation of magneto devices such as, for instance, Landau level lasers [11], without requiring a large magnetic field.

The control of strain, however, remains a challenging goal. The aim of this thesis is the creation and the study of different strain profiles induced in free-standing graphene by applying a pressure load to a micropatternd SiN membrane with pass-through holes of different sizes and shapes, onto which monolayer graphene has been anchored. The effects induced by strain were studied by micro-Raman spectroscopy as a function of the shape and the size of the holes, as well as of the applied pressure load.

The present thesis is divided in two main sections. The first part contains a general introduction to graphene and its mechanical properties, the theoretical principles behind the chosen measurement techniques, and an experimental review of strain in graphene. The second part is focused on the experimental work done during the thesis and on the obtained results.

In particular, a general description of the graphene structure and its electronic properties is given in Chapter 2 (section 2.1). Different growth techniques are also reviewed (section 2.2), with a focus on chemical vapor deposition (CVD), which was used to prepare the monolayer graphene analyzed in this thesis. The definitions of the quantities necessary to describe the mechanical response of graphene, such as the strain and stress tensors, the Young modulus and the Poisson ratio, are introduced in Chapter 3. The description of the Raman spectroscopy technique is given in Chapter 4: the origin of the Raman peaks in the spectrum of monolayer graphene is explained in section 4.1, while section 4.2 addresses their evolution in the presence of uniaxial and biaxial strain, which include a marked redshift in both the G and $2D$ Raman peaks. An experimental review regarding the present status of the investigation of strain in graphene is also reported.

The second part of the thesis focuses on the original experimental work performed during the present master project, and is described in Chapter 5: after illustrating the procedure for both the production of micropatterned SiN membranes (subsection 5.1.1) and the deposition of graphene on the samples (subsection 5.1.2), the setup used to perform the micro-Raman measurements is described (section 5.2), as well as the details of the Raman experiments (subsection 5.3.1). Subsequently, the procedure used to elaborate the data is discussed, also on the basis of numerical simulations developed during this thesis work (subsection 5.3.2). The final part of the chapter focuses on the analysis and discussion of the experimental results (subsection 5.3.2): a special attention is devoted to the study of the spatially-resolved mapping of redshifted $2D$ and G Raman peaks over the free-standing graphene, as indication of the finite value of the hydrostatic component of strain. In addition, Raman maps have been analyzed as a function of the hole geometries and of their dimensions: based on the non-trivial evolution of the linewidth of the G peak and from its splitting, it has been possible to

demonstrate the presence of an anisotropic component of the strain in the devices with elliptical holes. Moreover, the dependence of the strain on the pressure load applied to the membranes has been investigated, providing a novel estimate of the Grüneisen parameters [12–14].

In Chapter 6, the discussion shifts to future perspectives for the implementation of active devices for graphene strain engineering, such as SiN membranes with electrostatic "comb" actuators (section 6.1) and MEMS stretchers (section 6.2). Finally, in Chapter 7, obtained results and final conclusions are summarized and discussed.

Graphene

Since its discovery in 2004 by K. Novoselov and A. Geim, graphene, an allotrope of carbon, has drawn the attention of the scientific world not only for its two-dimensional nature but also for its surprising properties, including the peculiar structure of its energy bands, its electronic properties, robustness and flexibility, which make it appealing for both practical applications and fundamental physics studies [1, 4].

2.1 Structure and properties

Graphene consists of carbon atoms arranged in a honeycomb lattice (Fig. 2.1a), which can be formally described as a triangular lattice with two atoms per unit cell or, equivalently, as two interpenetrating triangular sublattices, which are conventionally labeled in the literature as A and B and disposed as shown in Fig. 2.1c [15]. The position of carbon atoms in a sublattice can be specified through the *primitive translation vectors*

$$\vec{a_1} = \frac{a}{2}(3, \sqrt{3}) \quad \vec{a_2} = \frac{a}{2}(3, -\sqrt{3}) \tag{2.1}$$

where $a \approx 1.42\,\text{Å}$ is the carbon-carbon distance. The position of the carbon atoms in the triangular sublattice is univocally determined by a linear combination $\vec{t_m} = m_1\vec{a_1} + m_2\vec{a_2}$, where m_1 and m_2 are integer numbers. The entire graphene hexagonal lattice can be obtained by the combination of the A and B sublattices, where the latter is traslated by a vector $(0, a)$ with respect to the former. This implies that each atom in sublattice B has three nearest neighbors, with relative positions

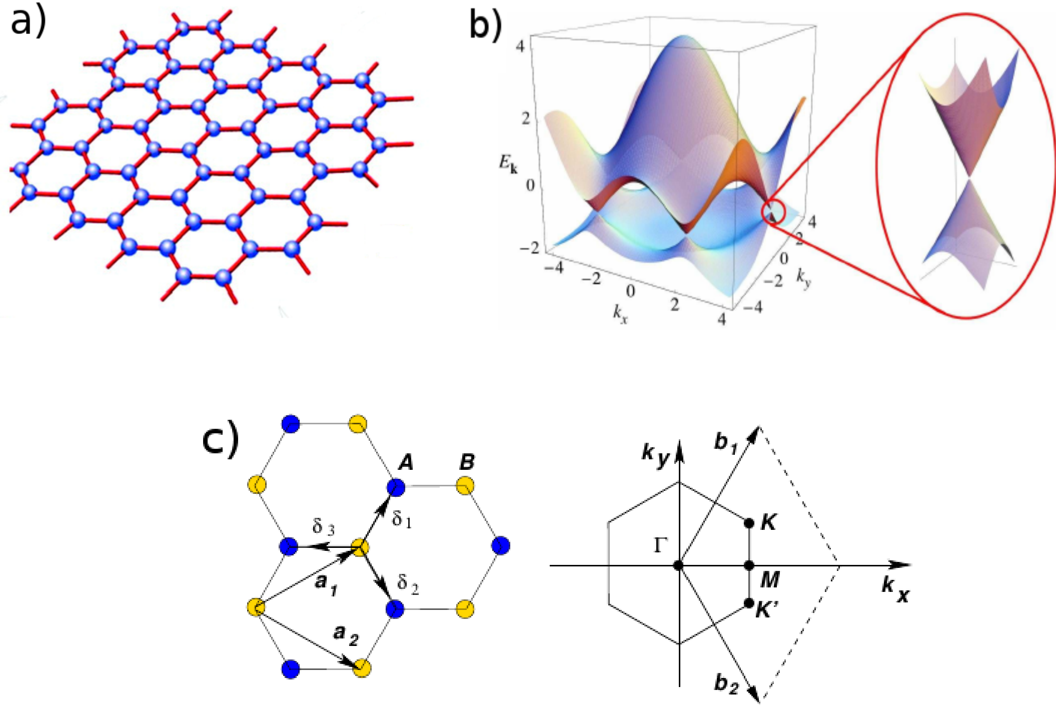

Figure 2.1: (a) Scheme of graphene honeycomb lattice. (b) Scheme of graphene electronic bands, with a zoomed view of the Dirac cone near the K point. (c) Scheme of the direct lattice, made up of two sublattices overlapping, and of the first Brillouin zone in k-space. Pictures taken from [15].

$$\vec{\delta_1} = \frac{a}{2}(1, \sqrt{3}) \quad \vec{\delta_2} = \frac{a}{2}(1, -\sqrt{3}) \quad \vec{\delta_3} = -a(1, 0) \tag{2.2}$$

As shown in Fig. 2.1c, the nearest neighbors of each carbon atom in the triangular lattice belong to the other sublattice. The *primitive reciprocal vectors* used to describe the reciprocal space shown in Fig. 2.1c are

$$\vec{b_1} = \frac{2\pi}{3a}(1, \sqrt{3}) \quad \vec{b_2} = \frac{2\pi}{3a}(1, -\sqrt{3}) \tag{2.3}$$

Within the first Brillouin zone, the two high symmetry points K and K', which are called *Dirac points* and have coordinates $K = \frac{2\pi}{3a}(1, \frac{1}{\sqrt{3}})$ and $K' = \frac{2\pi}{3a}(1, -\frac{1}{\sqrt{3}})$, are crucial in the description of electronic properties of graphene. Furthermore, it is important to notice that K and K' points are not connected by any vector of the reciprocal lattice and are therefore not equivalent in the momentum space.

The band structure of graphene can be described using the tight-binding method,

which approximates the crystal states as a combination of localized atomic orbitals of the lattice sites, plus a nearest-neighbor hopping Hamiltonian which takes the form [15] ($\hbar$=1 units)

$$H = -t \sum_{\langle i,j \rangle, \sigma} \left(a^{\dagger}_{\sigma,i} b_{\sigma,j} + h.c. \right) \tag{2.4}$$

where $a^{\dagger}_{i,\sigma}$ ($b^{\dagger}_{j,\sigma}$) and $a_{i,\sigma}$ ($b_{j,\sigma}$) are the creation and annihilation operators for an electron with spin $\sigma = (\uparrow, \downarrow)$ in the i-th (j-th) site in sublattice A (B). The sum is performed so that the j-th index runs over all the nearest-neighbors of the i-th site. Experimentally, the *nearest neighbor hopping energy* t is found to be equal to $t \approx 2.8\,\text{eV}$.

Each carbon atom is endowed with 6 electrons: two of them fill the core 1s orbital; the other four are responsible for the creation of the hexagonal backbone of graphene and of the conduction and valence bands. These can be described in terms of the 2s, 2p$_x$, 2p$_y$ and 2p$_z$ orbitals. In particular, 2s, 2p$_x$, 2p$_y$ hybridize into sp^2 orbitals, which overlap with orbitals of the same type belonging to the nearest neighbor atoms and form strong σ bonds responsible for graphene's mechanical properties. The σ bands are completely filled, and form deep valence bands. The remaining 2p$_z$ orbital, which is perpendicular to the lattice plane, is at the origin of the lowest conduction band and the highest valence band [15, 16]. The band dispersions can be obtained starting from the hopping hamiltonian of equation (2.4) and diagonalizing it in terms of Bloch states with two independent components over the A and B sublattices, which can be described in terms of a *pseudospin* degree of freedom. The resulting eigenenergies as a function of the wave vector $\vec{k} = (k_x, k_y)$ are

$$\begin{aligned} E(\vec{k}) &= \pm\sqrt{3 + f(\vec{k})} \\ f(\vec{k}) &= 2\cos(\sqrt{3}k_y a) + 4\cos\left(\frac{\sqrt{3}}{2}k_y a\right)\cos\left(\frac{3}{2}k_x a\right) \end{aligned} \tag{2.5}$$

where the plus and minus signs correspond to the conduction and valence bands, which are degenerate at the K and K' points. A low-energy limit for these dispersions can be obtained by rewriting the wavevectors as $\vec{k} = \vec{K} + \vec{q}$ where $\vec{K}$ is the position of the K

(or K') point. The hamiltonian can be expanded for small $|\vec{q}|$ around the K point as

$$H_K = v_F \begin{bmatrix} 0 & q_x - iq_y \\ q_x + iq_y & 0 \end{bmatrix} \tag{2.6}$$

where $v_F = |3ta/2| \sim 10^6$ m/s corresponds to the electron *Fermi velocity*. Near the K and K' points, the low-energy Hamiltonian mimicks the Dirac equation, implying that electrons in graphene behave formally like relativistic particles with a rest mass equal to zero, but with a velocity $v_F \approx c/300$ instead of the speed of light. Besides, eigenenergies are clearly $E(\vec{q}) = \pm v_F|\vec{q}|$ depending on whether the pseudospin points in the same or opposite direction with respect to $\vec{q}$, i.e. depending on the pseudo-helicity. This peculiar band structure gives rise to the characteristic linear dispersion of electrons in graphene and is at the base of its exceptional electronic mobility [15].

2.2 Production of graphene

The most common techniques to obtain high quality monolayer graphene are (i) micromechanical cleavage from bulk graphite and (ii) growth by either thermal decomposition of silicon carbide SiC or chemical vapour deposition (CVD). Examples of flakes obtained with these methods are reported in Fig. 2.2.

Exfoliation was used by Nobel prizes K. Novoselov and A. Geim when they first isolated graphene [1]. This method is still one of the most commonly used because it is relatively simple to implement and can yield a material with a very low density of defects and high electron mobility. Single layers of graphene can be obtained from bulk graphite using adhesive tape: a small piece of graphite is placed on the adhesive tape, which is then folded and unfolded multiple times in order to mechanically separate the stacked layers making up the graphite sample. The exfoliated flakes on the tape are then deposited on a Si wafer covered by a SiO_2 layer, whose thickness is crucial for the visibility of monolayer flakes [17, 18]. Graphene color on SiO_2 is in fact due to reflectivity of Si and to multiple reflections within the oxide thin film, giving rise to interferometric colors that depend in a sensitive way on the transparency of the air-SiO_2 interface. This effect becomes particularly visible to the human eye for few selected

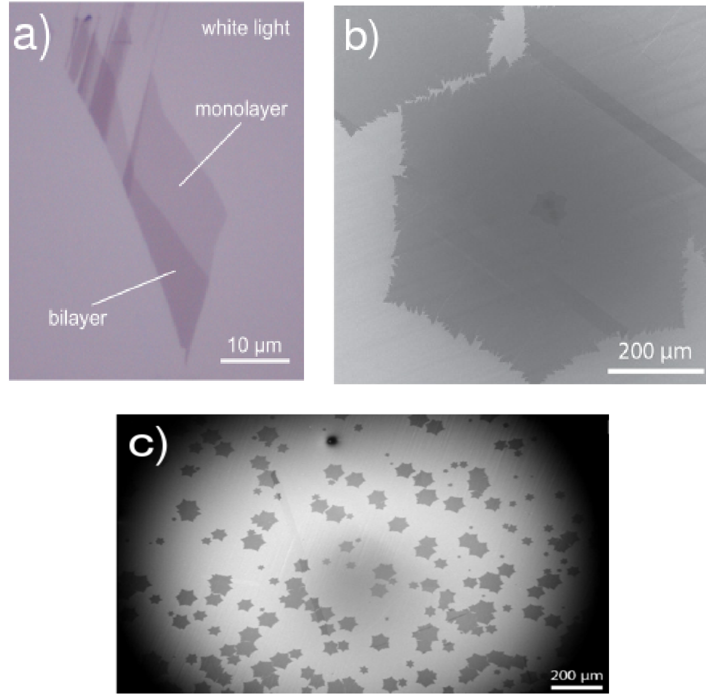

Figure 2.2: (a) Optical image of monolayer and bilayer graphene, showing their different contrast. (b) SEM image of a monolayer graphene flake grown by CVD [19]. (c) SEM image of graphene flakes grown by CVD over a flat Cu foil [19].

oxide thickness ranges. Among these, $280-300$ nm is a very common choice. Depending on the color of the flakes, one can preliminarily establish whether the graphitic material is a monolayer, a bilayer or multilayer (see Fig. 2.2a). Using mechanical exfoliation, it is possible to obtain graphene samples up to sizes of the order of $100\,\mu$m, even though the technique doesn't allow control over the dimension of the produced flakes.

Growth by thermal decomposition of SiC and by CVD allows the creation of graphene samples of large dimensions, up to several millimeters, with a low defects density and a good crystalline quality. CVD growth, in particular, allows to obtain large scale monocrystals, with a good control over the size and the density of the flakes. Due to these good properties, CVD was selected to prepare the graphene used for the device studied during this thesis work (see Chapter 5).

CVD growth exploits transition metals, usually copper (Cu), as a catalyst for a surface-mediated decomposition of the percursor gas (typically CH_4) and for the creation of large homogeneous films of graphene. As described in Ref. [19], a high purity Cu foil is electropolished to reduce its surface roughness and is inserted into the CVD furnace, which is first evacuated and then heated up to a temperature of about 1000°C.

Subsequently, H_2 or Ar is used in an annealing process to clean the metal surface from contamination. Once the copper foil has been heated close to its melting point, a constant flux of CH_4 is released inside the chamber: the gas reacts with the heated metal, dissociates and releases its carbon atoms, which become mobile on the copper surface, where they can form the well-know hexagonal lattice of graphene. After an arbitrary amount of time, that can range from one minute up to a few hours and is chosen according to the desired dimension of the flakes, the chamber is cooled down and the graphene on copper can be extracted from the CVD furnace.

The choice of the deposition parameters is crucial for the graphene synthesis process: a longer or shorter growth time allows to choose between a sample constituted by a continuous film of polycrystalline graphene or by several isolated monocrystalline flakes (Fig. 2.2c). In the former case, the density and size of the flakes can be controlled through the growth pressure and time (Fig. 2.2b). The quality of the copper foil used for the growth is also crucial to determine the quality of the synthesized graphene: for instance a rough substrate can induce ripples on the flakes, which could impact its intrinsic strain and alter its optical properties.

Mechanical deformation of graphene

3.1 Introduction to continuum mechanics

Continuum mechanics is a branch of mechanics that deals with the deformation and the mechanical response of continuous solid bodies.

A generic modification of the configuration of a solid body, caused for example by an external load, can be described using either the *body coordinate system* $\vec{X}$ or the coordinates $\vec{x}(\vec{X}, t)$, representing the actual position of the body's material points after the movement. The latter is named *Langrangian coordinate system*, since it describes the body in terms of its undeformed configuration. In order to study a generic deformation, it is useful to define the *displacement vector field*

$$\vec{u}(\vec{X}, t) = \vec{x}(\vec{X}, t) - \vec{X} \tag{3.1}$$

which relates the deformed and undeformed configuration of the body. For the description of its mechanical response, the relative shift of each point with respect to the adjacent ones, i.e. the variation of the displacement as a function of the body coordinates, is of great relevance and can be quantified by the *deformation gradient*

$$F_{ij} = \frac{\partial x_i}{\partial X_j} = \frac{\partial u_i}{\partial X_j} + \delta_{ij}. \tag{3.2}$$

The term $\partial_{X_i} u_j$ is named *displacement gradient* and associates an infinitesimal distance in the undeformed system $d\vec{X}$ to the respective distance $d\vec{x}$ in the deformed one though the expression $dx_i = F_{ij} dX_j$.

The definition of equation (3.2) is general and can be used to describe any variation in the body's configuration, including those due to translations, rotations and deformations alike. The local deformation of the object can be described by the quadratic form of the *Green-Lagrange strain tensor*, defined as

$$\epsilon_{ij} = \frac{\partial_{X_i} u_j + \partial_{X_j} u_i + \partial_{X_i} u_k \partial_{X_j} u_k}{2}. \tag{3.3}$$

The strain tensor is symmetric, thus it contains only six independent degrees of freedom; furthermore, for every given position, it can be diagonalized by an appropriate choice of the coordinate system, so that any arbitrary deformation can be locally seen as due to compression/elongation along three mutually orthogonal axis.

3.2 Small deformation limit and linear elastic response

In the limit of small deformations, which holds when the displacement gradient is smaller than unity, i.e. $|\vec{\nabla}\vec{u}| \ll 1$, the strain tensor can be rewritten as

$$\epsilon_{ij} \approx \frac{\partial_{X_i} u_j + \partial_{X_j} u_i}{2}. \tag{3.4}$$

Its meaning is better understood considering the trivial example of a cube of side L where a constant force F is applied to one of its faces, so that it is deformed as in Fig. 3.1a. If the length of the cube along the x axis is increased by a quantity ΔL_x, the displacement of each point along the same direction is equal to $u_x = \Delta L_x \cdot (x/L_x)$. The factor relating the displacement of the point to its position inside the body is an element of the strain tensor, that can be defined as $\epsilon_{xx} = \Delta L_x / L_x$. Its expression can be generalized for non homogeneous strains as $\epsilon_{xx} = \partial u_x / \partial x$ and the definition can be extended to the other diagonal elements $\epsilon_{yy} = \partial u_y / \partial y$, $\epsilon_{zz} = \partial u_z / \partial z$. In more general cases, when the strain axes do not correspond to the ones of the coordinate system, off-diagonal elements of the strain tensor are necessary to completely describe the deformation of the body. An example of a shear deformation is given in Fig. 3.1b: the displacement of a material point along the x axis depends on the coordinate along

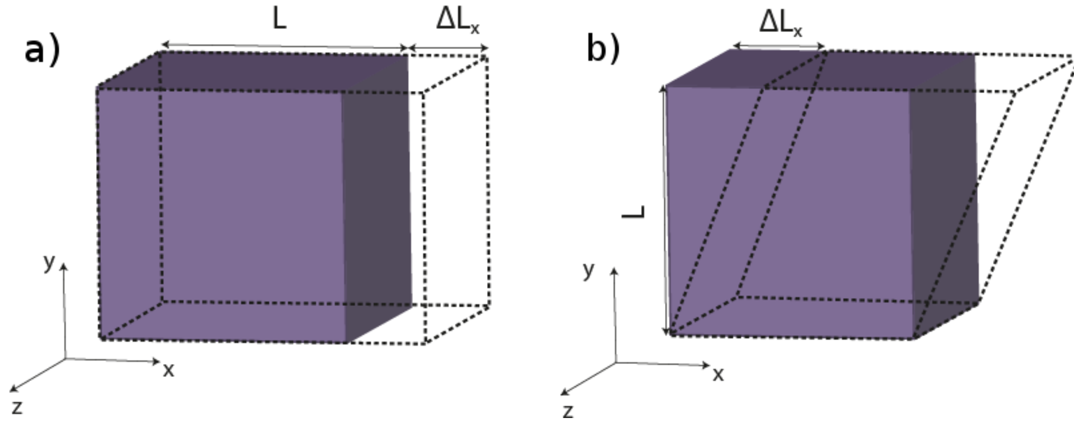

Figure 3.1: Sketch of a cubic material subject to (a) normal deformation along the x direction and (b) shear deformation along the xy direction.

the y direction, yielding $u_x \propto (y/L_y)$ and a non-zero off-diagonal strain tensor element $\epsilon_{xy} = \partial u_x / \partial y$.

The relation between the body strain configuration and its elastic response can be described starting from the Lagrangian of the system

$$L = \int \left[\frac{1}{2} \rho_0 \cdot \left(\dot{\vec{x}} \right)^2 - w(\epsilon) \right] d^3 \vec{X} \tag{3.5}$$

where $\rho_0(\vec{X})$ is the mass density of the body and $w(\epsilon)$ is the potential energy density, which is a function of the deformation tensor. After introducing the *Cauchy stress tensor* σ, as $\sigma_{ij} = \partial w / \partial \epsilon_{ij}$, the resulting Eulero-Lagrange equation for a continuous body assumes the form

$$\rho_0 \ddot{\vec{x}} = \vec{f} + \frac{\partial \sigma_{ij}}{\partial x_i} \vec{e_j} = \vec{f} + \vec{\nabla} \cdot \vec{\sigma} \tag{3.6}$$

where f are the external forces per unit volume applied to the body. The physical meaning of the stress tensor can be seen integrating equation (3.6) over a generic volume Ω inside the material, which yields

$$\vec{F} = \int_{\Omega} \vec{f} dV + \int_{\partial \Omega} \sigma_{ij} dS_j . \tag{3.7}$$

From equation (3.7) it is possible to see that, along with the external ones, every given volume of the material is subject to a force, applied on its surface and typically

named *traction*, taking the infinitesimal form $d\vec{T} = \sigma d\vec{s}$. This force describes the internal stress of the material arising from the deformation and is applied between adjacent regions of the same object. Its direction, for a given surface element, is described by the stress tensor and can include both normal and shear components.

For linear elastic bodies and for small deformations, the Hooke approximation can be applied. According to it, the stress tensor is proportional to the strain and their components are related by the expression

$$\sigma_{ij} = \sum_{k,l} C_{ijkl}\epsilon_{kl} \tag{3.8}$$

where C is a rank-four tensor, named *tensor of elasticity.* In this first-order limit, in fact, the elastic potential energy stored in the material can be approximated as a quadratic form of the strain tensor elements [20]

$$w = \frac{1}{2}\sum_{i,j,k,l,} C_{ijkl}\epsilon_{ij}\epsilon_{kl}. \tag{3.9}$$

In homogeneous and isotropic materials, thanks to the symmetries of the strain tensor, the elements of the tensor of elasticity can be written as

$$C_{ijkl} = \lambda\delta_{ij}\delta_{kl} + \mu(\delta_{ik}\delta_{jl} + \delta_{il}\delta_{jk}) \tag{3.10}$$

and then used to simplify equation (3.8), giving its final form

$$\sigma_{ij} = 2\mu\epsilon_{ij} + \lambda Tr[\epsilon]\delta_{ij} \tag{3.11}$$

where μ and λ are called Lamé parameters.

These coefficients can be related to other phenomenological elastic parameters that describe the mechanical response of an isotropic material under stress, such as the *Young modulus* E and the *Poisson ratio* ν

$$\lambda = \frac{\nu E}{(1-2\nu)(1+\nu)} \qquad \mu = \frac{E}{2(1+\nu)} \tag{3.12}$$

Their definition can be obtained using the example of the cube under strain reported

in Fig. 3.1a: when a constant force is applied to one of the cube faces, while the body is stretched along the force direction of a quantity ΔL_x, at the same time it generally shrinks laterally by a quantity ΔL_y and ΔL_z. The magnitude of the length variation along the directions perpendicular to the strain is given by the *Poisson ratio*, defined as $\nu = -\epsilon_{yy}/\epsilon_{xx} = -\epsilon_{zz}/\epsilon_{xx} = -\Delta L_y/\Delta L_x = -\Delta L_z/\Delta L_x$. Most of materials display $\nu \geq 0$ and $\nu \leq 0.5$ (a strict limit reached for incompressible solids). The Young modulus describes the elastic response of the body to the external force applied, and relates it to the strain tensor through the expression $P = E \cdot \epsilon_{xx}$, where P is the force for unit area applied to the cube.

Raman spectroscopy as an analysis tool for graphene

Raman spectroscopy is a non-destructive optical technique that allows obtaining information about the chemical composition and the structure of a material by observing of its vibrational and rotational modes.

Unlike in Rayleigh scattering, optical transitions in Raman scattering are due to an inelastic process: the incident and emitted photons do not have equal energy and they are relatively shifted by the energy quantum of a vibrational mode, which is either excited or de-excited. When the incident light interacts with the sample, the latter is excited to a virtual state (see dotted line in the energy diagram of Fig. 4.1) by absorbing the incident photon at energy $E_L = \hbar\omega_L$. The virtual state is not a stationary state and it immediately relaxes back to one of the stable vibrational configurations, by emitting a photon at energy $E_s = \hbar\omega_s$. Depending on the initial and final vibrational state of the sample, different scattering processes can take place:

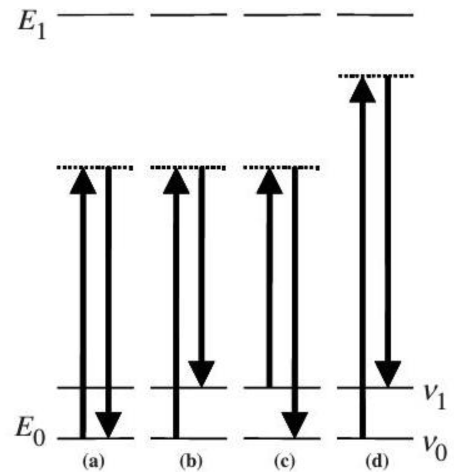

Figure 4.1: Scheme of the (a) Rayleigh, (b) Stokes Raman, (c) anti-Stokes Raman scattering process and of the (d) Stokes Raman scattering process using a different excitation wavelength. Picture taken from [21].

I) *Rayleigh scattering*: the material returns to the same initial vibrational level, so the scattered photon has the same energy of the incident one, i.e. $E_s = E_L$ (Fig. 4.1a).

II) *Stokes Raman scattering*: a vibration quantum $\hbar\omega_v$ is excited during the light scattering process, thus the emitted photon is less energetic than the incident one $E_s = E_L - \hbar\omega_v$ (Fig. 4.1b).

III) *anti-Stokes Raman scattering*: a vibration quantum $\hbar\omega_v$ is de-excited during the light scattering process, thus the emitted photon is more energetic than the incident one $E_s = E_L + \hbar\omega_v$ (Fig. 4.1c).

After filtering out the light generated by Rayleigh scattering, by blocking the radiation with the same wavelength of the incident laser light, Stokes and anti-Stokes Raman scattered radiation is used to obtain the Raman spectrum as a function of the *Raman shift* Δw, which is measured in cm^{-1} and defined as

$$\Delta w = \left(\frac{1}{\lambda_L} - \frac{1}{\lambda_s}\right) \tag{4.1}$$

where λ_L is the excitation wavelength and λ_s is the scattered light wavelength. According to the quantum mechanical description of the Raman scattering process, the intensity of the Raman scattered light can be obtained from the expression [21]

$$I_R = \frac{16\pi^3}{405c^4} \frac{hI_L N(\nu_L - \nu)^4}{\mu\nu(1 - e^{-h\nu/kT})}[45(\alpha_a)^2 + 7(\gamma_a)^2] \tag{4.2}$$

where c is the speed of light, h the Planck's constant, N the number of quasi-particles that are affected by Raman scattering, I_L and ν_L the intensity and frequency of the incident radiation, ν the mechanical vibration frequency, μ the reduced mass of the vibrating mode, k the Boltzmann's constant, T the temperature measured in Kelvin, α_a the mean value invariant of the polarizability tensor and γ_a its anisotropy invariant.

Equation (4.2) allows describing some of Raman spectroscopy's main features: the intensity of the Raman signal is, as expected, directly proportional to the intensity of the incident light but also to the number of scattering centers, making Raman spectroscopy suitable for quantitative analysis aimed at studying the variation of concentrations in the sample. The dependence of the intensity from both the main value invariant of the polarizability tensor and from its anisotropy invariant allows to use Raman spectroscopy as a tool to study the crystal orientation of a sample. Indeed, in a semiclassical limit, the Raman scattering process can be seen as the interaction between the electromagnetic

field of the incident light and the electrons of the chemical bond: radiation excites the material into the virtual state and induces a dipole moment with a direction determined by the light polarization, via the polarizability tensor. The induced dipole moment is in turn responsible for light re-emission. The amplitude of the Raman resonances can thus be expected to depend on the exact polarization of the laser light.

4.1 Raman spectra of mono-layer graphene

The peculiar features of Raman spectroscopy and its non destructive nature make it a versatile tool for studying graphene, and allow obtaning information not only on its phononic dispersion, but also on the number of layers, on the orientation and the type of the crystal edges [22–24], on the presence of defects and doping [25–27] and on the effects of external perturbations such as strain, electric and magnetic field [12–14, 28–33].

In order to analyze and interpret correctly the Raman spectra of monolayer graphene, it is fundamental to understand the origin of each peak and its relation to the graphene phonon dispersion. The presence of two carbon atoms in each unit cell of the lattice results in six phonon dispersion branches, three acoustic one (indicated by the letter A) and three optical ones (O). Based on the direction of the atomic vibration with respect to the phonon wave vector $\vec{q}$, phonon branches can be classified either as longitudinal (L) or as transverse (T), according to vibrations parallel or perpendicular to $\vec{q}$. Transverse phonons can be further divided into out-of-plane (o) transverse modes, if the vibration direction is perpendicular to graphene's plane, and in-plane (i) ones if the vibration occurs in the graphene's plane. The six phonon dispersion branches, with their respective labels, are shown in Fig. 4.2a.

The phonons involved in Raman scattering processes have to satisfy both energy and momentum conservation laws, which lead to the so-called *fundamental Raman selection rule* [25]. Based on the number of phonons involved in the process (one, two or more), Raman scattering can be classified as first order, second order or higher. In first-order Raman, the following conservation laws need to be satisfied

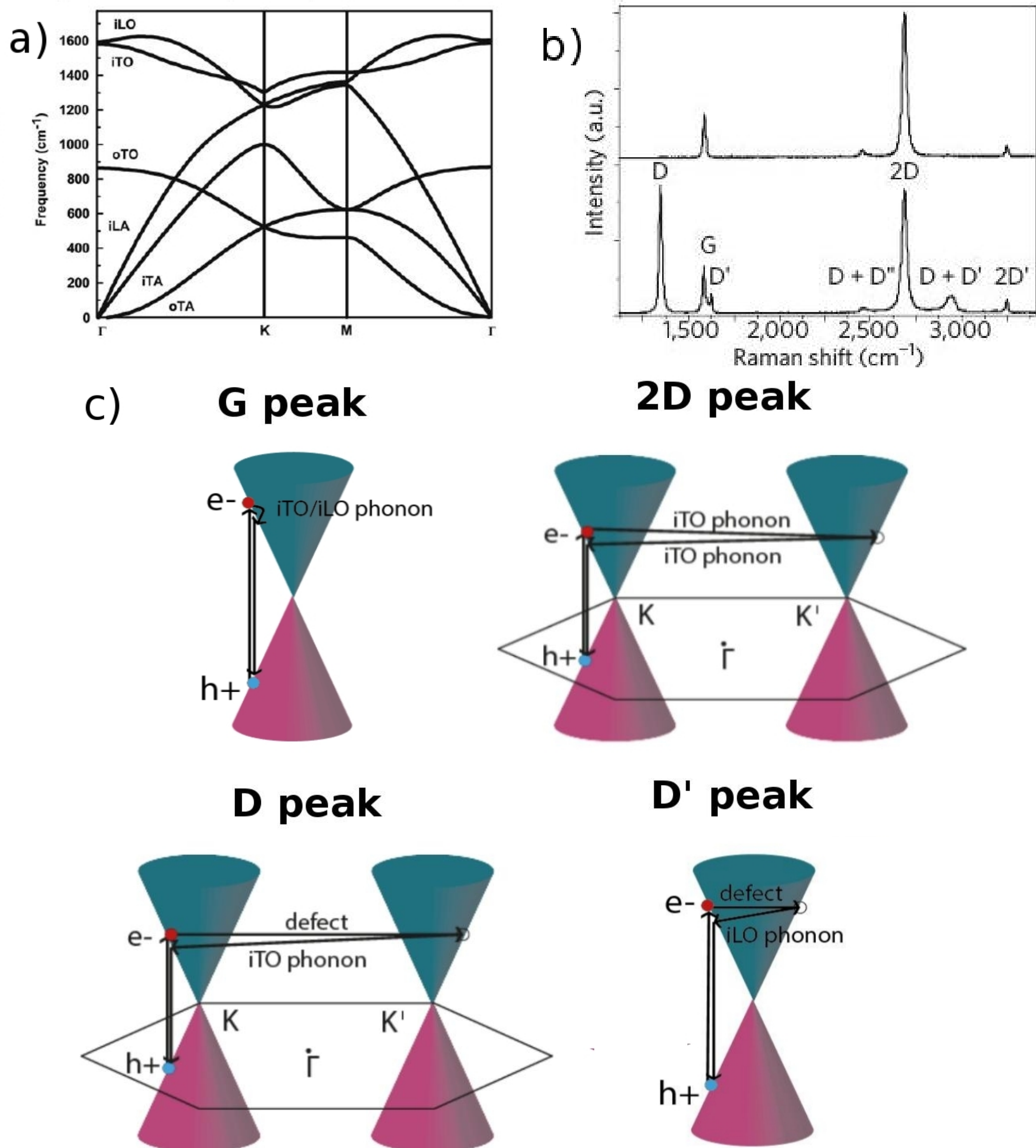

Figure 4.2: Raman spectrum of monolayer graphene. (a) Phonon dispersion relation of monolayer graphene: longitudinal acoustic (iLA) and optic (iLO) phonon branches; transverse acoustic (iTA and oTA) and optic (iTO and oTO) phonon branches. Picture taken from [27]. (b) Raman spectra of graphene samples both with defects (bottom) and without (top). Picture taken from [25]. (c) Sketch of the fundamental scattering processes relevant to the creation of the G, D, D' and $2D$ peak, as described in Ref. [27].

$$\vec{k_L} = \vec{k_s} \pm \vec{q} \qquad \hbar\omega_L = \hbar\omega_s \pm \hbar\omega_v(\vec{q}, b) \tag{4.3}$$

where ω_L, ω_s, $\omega_v(\vec{q}, b)$ are the frequencies of the incident laser photon, the scattered one and of the phonon belonging to the branch b and of wave vector $\vec{q}$ involved in the scattering process. Similarly, k_L, k_s, $\vec{q}$ indicate the respective wave vectors. Since the wavelength of the incident light used in Raman experiments generally belongs to the visible spectrum (i.e. it is included between 1000 nm and 300 nm) and given the value of the lattice parameters determining the dimensions of the Brillouin zone ($a \approx 1.42\,\text{Å}$), optical transitions are almost vertical in the reciprocal space and $k_L, k_s \ll \pi/a$. This implies a similar relation has to hold for phonons involved in first-order Raman scattering as well: $|\vec{q}| \ll \pi/a$ and thus $|\vec{q}| \approx 0$.

Raman peaks in graphene are conventionally labeled according to the type of phonons and the order of the Raman scattering involved:

(I) *G Peak*: in graphene without defects, this is the only peak resulting from a single-phonon scattering process (see Fig. 4.2c) and it is observed at $\Delta w \sim 1580\,\text{cm}^{-1}$. Because of Raman selection rules, the only phonons contributing to scattering are the iTO and iLO modes at the Γ point, which correspond to a relative vibration of the two crystal sublattices. The study of the G peak is also useful to gain an insight on graphene's doping, which impacts the peak parameters, in particular the energy position.

(II) *2D Peak*: it is the second prominent feature of the Raman spectrum of clean graphene and it is due to a second-order Raman scattering. It is observed at $\Delta w \sim 2685\,\text{cm}^{-1}$. According to the fundamental selection rule, in principle every couple of phonons with opposite wave vectors can contribute the second-order Raman scattering. In practice, only phonons near the Γ or the K point dominate the Raman response [27, 34, 35]. The latter case, referred to as *intervalley* second order Raman scattering (shown in Fig. 4.2c) and involving the iTO phonon mode near the K point, is responsible for the $2D$ resonance.

The $2D$ peak is particularly relevant since its lineshape changes strongly in multilayer graphene with respect to the monolayer case: Van der Waals interaction between

the layers modifies the phonon bands by splitting them, thus allowing a larger number of intervalley scattering processes to occur. This results in a peculiar broadening of the $2D$ peak that allows discriminating the number of layers.

(III) *D and D' Peak*: they are typically observed in disordered graphene and they result from Raman scattering process mediated by elastic scattering on a defect (see Fig. 4.2c). They are observed at $\Delta w \sim 1360\,\mathrm{cm}^{-1}$ and $\sim 1620\,\mathrm{cm}^{-1}$, respectively. The D' peak involves the iLO phonon mode close to the Γ point, which induces an intravalley scattering. The D peak involves the iTO phonon mode close to the K point, which induces an intervalley scattering. As suggested by the spectra in Fig. 4.2b, their intensity is proportional to the density of defects, while in high-quality samples they are absent.

Since the physical edge of the graphene flake can play a similar role to defects, in breaking the strict conservation of the momentum, the analysis of the intensity of the D peak, as well as of the G peak as a function of the polarization of the incident light, can be used to obtain information about the type of edge, either armchair or zigzag, and thus on the orientation of the lattice [22–24].

4.2 Uni-axial and bi-axial strain effects on graphene's Raman spectra

Raman spectroscopy has proven to be a useful tool to study graphene's phonon structure and thus to investigate the changes induced by external perturbations. For example, the presence of strain breaks the hexagonal symmetry of the lattice and modifies phononic modes, resulting ultimately in the shift of Raman peaks, in particular the G peak.

The relation between the applied strain and the resulting shift of the peaks near the Γ point can be obtained from the dynamical equation describing the normal phononic modes involving the relative oscillations of the two graphene sublattices [28, 36]

$$\sum_{\beta} K_{\alpha\beta} u_{\beta} = \omega^2 u_{\alpha} \tag{4.4}$$

where $\vec{u} = (u_1, u_2)$ is the relative displacement of the two carbon atoms inside the unit

cell, ω is the phonon frequency and $K_{\alpha\beta}$ are the elements of the force constant tensor. In the presence of a strain ϵ, they can be expanded for small perturbation as

$$
\begin{aligned}
K_{\alpha\beta} &= K^0_{\alpha\beta} + \sum_{lm} K_{\alpha\beta lm}\epsilon_{lm} \\
K^0_{\alpha\beta} = \omega_0^2\delta_{\alpha\beta} \qquad K_{\alpha\beta lm} &= \frac{\partial K_{\alpha\beta}}{\partial \epsilon_{lm}}
\end{aligned}
\tag{4.5}
$$

where ω_0 is the phonon frequency of unstrained graphene and ϵ_{lm} are the elements of the strain tensor. Since the lattice has an hexagonal symmetry, $K_{\alpha\beta lm}$ is characterized by only two independent parameters A and B. In particular, $K_{1111} = K_{2222} = A$, $K_{1122} = B$, $K_{1212} = \frac{1}{2}(A - B)$ while all the other terms vanish. The secular equation for the phononic modes can be rewritten as

$$
\begin{vmatrix} A\epsilon_{xx} + B\epsilon_{yy} - \lambda & (A-B)\epsilon_{xy} \\ (A-B)\epsilon_{xy} & B\epsilon_{xx} + A\epsilon_{yy} - \lambda \end{vmatrix} = 0 \tag{4.6}
$$

where $\lambda = \omega^2 - \omega_0^2$. The solution of the secular equation takes the form

$$
\lambda = \frac{1}{2}\left((A+B)(\epsilon_{xx} + \epsilon_{yy}) \pm (A-B)\sqrt{(\epsilon_{xx} - \epsilon_{yy})^2 + 4\epsilon_{xy}^2} \right). \tag{4.7}
$$

An explicit expression of the shift can be obtained based on the definition of λ

$$
\begin{aligned}
\Delta\omega = \omega - \omega_0 &\approx \frac{\lambda}{2\omega_0} \\
\Delta\omega = \frac{(A+B)}{4\omega_0}(\epsilon_{xx} + \epsilon_{yy}) &\pm \frac{(A-B)}{2\omega_0}\sqrt{(\epsilon_{xx} - \epsilon_{yy})^2 + 4\epsilon_{xy}^2}.
\end{aligned}
\tag{4.8}
$$

The former equation can be rewritten using the *Grüneisen parameter* γ and the *shear deformation potential* β [30]

$$
\gamma = -\frac{1}{4\omega_0^2}(A+B) \qquad \beta = \frac{1}{2\omega_0^2}(A-B) \tag{4.9}
$$

The final form of equation (4.8) for the frequency shift of optical phonons as a function of the strain is

$$\boxed{\Delta\omega_G = -\gamma_G \omega_G^0(\epsilon_{xx}+\epsilon_{yy}) \pm \frac{1}{2}\beta_G\omega_G^0\sqrt{(\epsilon_{xx}-\epsilon_{yy})^2+4\epsilon_{xy}^2}}. \tag{4.10}$$

Even though the equation describes only the Raman peaks due to inelastic scattering involving phonons near the Γ point, i.e. G and D' peaks, a similar expression for the $2D$ peak can be written as [13]

$$\Delta\omega_{2D} = -\gamma_{2D}\omega_{2D}^0(\epsilon_{xx}+\epsilon_{yy}). \tag{4.11}$$

From equations (4.10) and (4.11), it is possible to describe the most important effects of strain on the Raman spectra: while biaxial strain induces only a shift in the peak positions ($\epsilon_{xx} = \epsilon_{yy} = \bar{\epsilon}$ and $\epsilon_{xy} = 0$), the presence of uniaxial strain is associated with a finite strain anisotropy $\Delta\epsilon = \sqrt{(\epsilon_{xx}-\epsilon_{yy})^2+4\epsilon_{xy}^2}$ and removes the degeneration of iTO and iLO phonon modes in the Γ point in the first Brillouin zone. This degeneracy lifting causes the G peak to split into two peaks, called G^- and G^+, generated by the new phonon modes parallel and perpendicular to the direction of the strain respectively, as shown in Fig. 4.3.

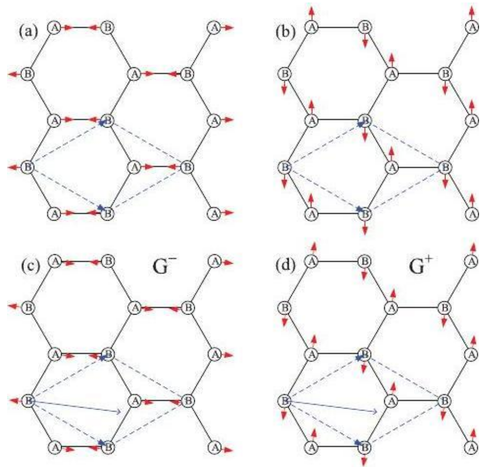

Figure 4.3: Atomic displacements for the doubly degenerate G mode (a) and (b), and the two split modes, G^-(c) and G^+(d), which are respectively parallel and perpendicular to the strain axis. Picture taken from [12].

4.3 Experimental evidences

Over the past few years, several experiments and theoretical papers have addressed the problem of the splitting of the G peak in graphene subjected to uniaxial strain, along with the shift of G and $2D$ Raman peaks under both uniaxial and biaxial strain. These phenomena have been quantified in terms of the corresponding Grüneisen parameters.

T.M.G. Mohiuddin *et al.* [13] investigated the impact of uniaxial strain by depositing graphene onto two different flexible substrates: (i) a 720 μm-thick and 23 mm-long

polyethylene terephthalate (PET) film and (ii) a 3 mm-thick and 10 cm-long clear acrylic sheet. Strain was induced by bending the substrates using either two and four pressure points. Both the splitting of the G peak and the shift of $2D$ and G peaks have been observed and the peak position as a function of the strain has been measured (see Fig. 4.4). The strain magnitude was estimated based on the ratio between the sample thickness and sample curvature radius. The experimental values obtained for the Grüneisen parameter and the shear deformation potential were $\gamma_G = 1.99$, $\beta_G = 0.99$ and $\gamma_{2D} = 3.5$. The peak shifts under uniaxial strain were found to be $\partial\omega_{G-}/\partial\epsilon \sim -36.4\,\text{cm}^{-1}/\%$, $\partial\omega_{G+}/\partial\epsilon \sim -18.6\,\text{cm}^{-1}/\%$, $\partial\omega_{2D}/\partial\epsilon \sim -83\,\text{cm}^{-1}/\%$. Experimental results were in agreement with values obtained from the simulation of graphene phonon bands under strain, except for the $2D$ Grüneisen parameter, which was expected to attain a value of ≈ 2.7.

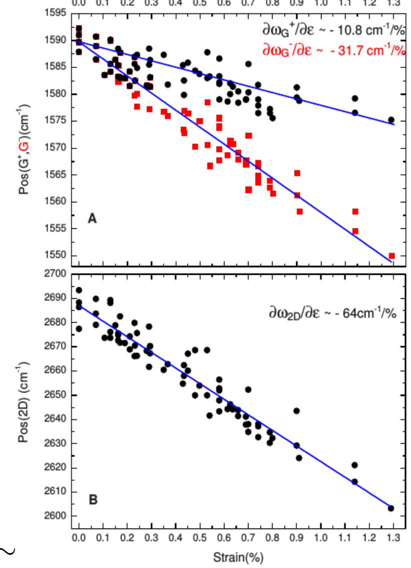

Figure 4.4: $2D$ and G peaks red-shift as a function of the applied strain, ranging from 0 to $\sim$1.3% which evidences the split of the G peak for uniaxial strain over 0.7% [13].

Huang *at al.* [28] specifically focused on the properties of the G peak under uniaxial strain and, from its splitting (see Fig. 4.5), they were able to obtain the experimental values of the elements of the force constant tensor: $A = (-4.4 \pm 0.8) \times 10^{-6}\,\text{cm}^{-2}$ and $B = (-2.5 \pm 0.5) \times 10^{-6}\,\text{cm}^{-2}$, see equation (4.8). Uniaxial strain was in this case induced by bending the PDMS film on which graphene was deposited and anchored with two Ti strips. The strain magnitude was directly measured based on the observed deformation of the metallic anchoring strips.

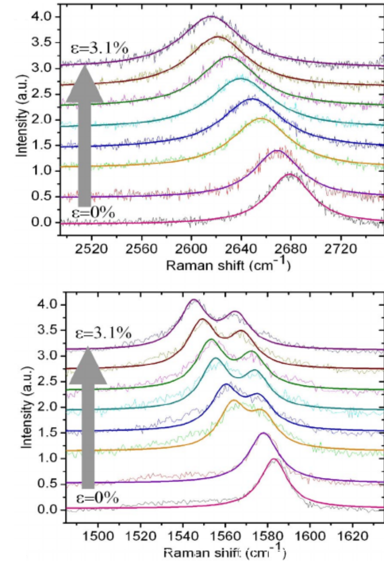

Figure 4.5: Evolution of the spectra of G and $2D$ Raman peaks under uniaxial strain, showing a clear split of the G peak at a strain of 1% [28].

Polyzos *et al.* [29] measured the effects of strain directly on suspended graphene, obtained by encap-

sulating a monolayer flake between two layers of PMMA and by subsequently freeing a rectangular region by e-beam lithography. Free-standing graphene was found to display a measurable strain due to the fabrication procedure: stress was accumulated in the PMMA layer during spinning on a Si substrate, onto which a second PMMA layer with graphene was deposited; when part of the PMMA was removed by lithography, such a stress was relieved, causing a visible deformation of the edges of the PMMA-free region and thus straining graphene. The Raman spectra acquired over the graphene sample showed not only the shift of the peaks, but also the splitting of both the G and $2D$ peak. The following experimental trends were observed: $\partial\omega_{G-}/\partial\epsilon \sim -37 \pm 2\,\mathrm{cm}^{-1}/\%$, $\partial\omega_{G+}/\partial\epsilon \sim -19 \pm 1\,\mathrm{cm}^{-1}/\%$, $\partial\omega_{2D_1}/\partial\epsilon \sim -84\,\mathrm{cm}^{-1}/\%$, $\partial\omega_{2D_2}/\partial\epsilon \sim -94\,\mathrm{cm}^{-1}/\%$ (see Fig. 4.6).

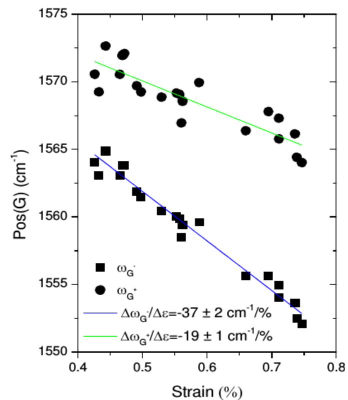

Figure 4.6: Position of G^+ and G^- peaks as a function of strain and their linear fit [29].

Zabel *at al.* [14] focused on the effects of biaxial strain on suspended monolayer and bilayer graphene. Strain was in this case applied through a differential pressure, obtained by anchoring graphene on a circular through hole on top of a chamber filled with nitrogen gas. The strain magnitude was estimated from the atomic force microscopy (AFM) topographic maps of the inflated graphene (see Fig. 4.7). The fit of the peak position plotted as a function of strain gives the following shift values $\partial\omega_G/\partial\epsilon \sim -57\,\mathrm{cm}^{-1}/\%$, $\partial\omega_{2D}/\partial\epsilon \sim -140\,\mathrm{cm}^{-1}/\%$. The obtained Grüneisen parameter for the $2D$ and G peak are $\gamma_G = 1.8$ and $\gamma_{2D} = 2.6$, in excellent agreement with the results already reported from T.M.G. Mohiuddin *et al.* [13].

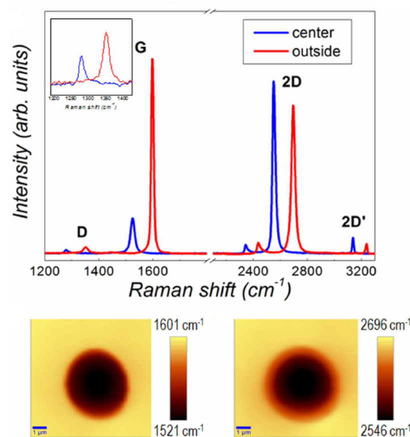

Figure 4.7: Comparison between spectra acquired at the center and outside a monolayer graphene bubble and Raman maps of G (left) and $2D$ (right) peak position under biaxial strain [14].

A further corroboration of the experimental values comes from the simulation of the phonon deformation potentials of graphene made by Y. C. Chen *et al.* [12]. Based on simulations of the phonon band structure of monolayer graphene subjected to small

strain, performed using ab initio pseudo-potential density functional-theory, the obtained trends yield $\partial\omega_{G^-}/\partial\epsilon \sim -34\,\mathrm{cm}^{-1}/\%$, $\partial\omega_{G^+}/\partial\epsilon \sim -17\,\mathrm{cm}^{-1}/\%$ for uniaxial strain and $\partial\omega_G/\partial\epsilon \sim -59\,\mathrm{cm}^{-1}/\%$ for biaxial strain (see Fig. 4.8). The following values for the Grüneisen parameter and the shear deformation potential have been calculated: $\gamma_G = 1.86$ and $\beta_G = 0.96$, both in good agreement with the experimental values.

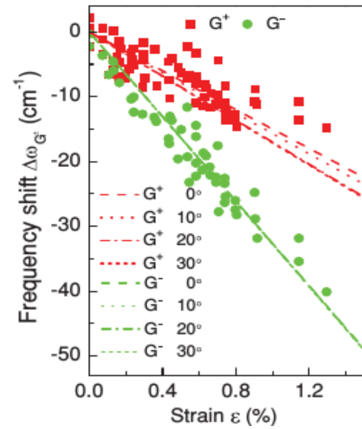

Figure 4.8: Shift of the G^+ and G^- with respect to the frequency of equilibrium of the simulated structure, together with the experimental data from Ref. [13], as a function of uniaxial strain [12].

Experimental results: Raman spectroscopy on deformed graphene

5.1 Sample fabrication

All sample fabrication processes were performed in an ISO6 class *cleanroom*, i.e. an environment with a controlled quantity of particles for cubic meter: in the specific case, less than 10^6 particles of $0.1\,\mu$m size or larger. The aim of the protocols described in the following is to obtain suspended graphene devices on patterned SiN membranes, which have been used to obtain and study different strain configurations and their effect on graphene. The process can be divided into two main phases: (i) the fabrication of the SiN membranes and (ii) the deposition of graphene.

A detailed description of the clean room equipment used in the fabrication process can be found in appendix.

5.1.1 SiN membranes fabrication

The production of the SiN membranes, as shown in Fig. 5.1, requires four main steps:

I. Back-side UV lithography;

II. SiN back-side reactive ion etching (RIE) and Si pre-etching;

III. Front-side e-beam lithography (EBL);

IV. SiN front-side RIE and final etching.

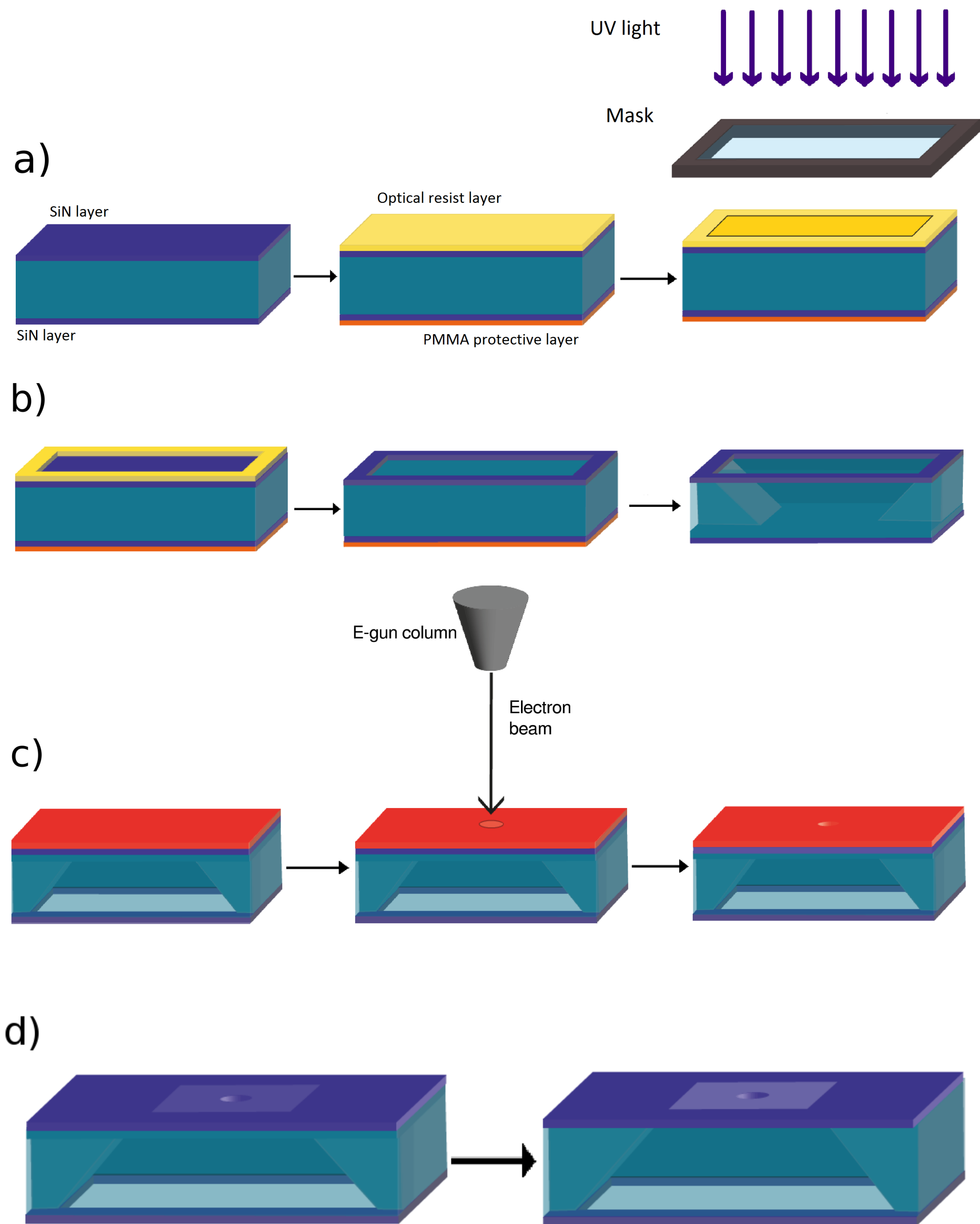

Figure 5.1: Sample preparation process flow. (a) Back-side UV lithography: after spin-coating PMMA on the front side of the sample and optical resist on the back one, the sample is exposed to UV light to create a pattern in the resist. (b) SiN back-side reactive ion etching (RIE) and pre-etching: after developing the exposed resist, a RIE process and a KOH solution are used to etch the exposed SiN and Si underneath, respectively. (c) Front-side EBL lithography: after applying a double layer of CSAR resist, the hole pattern is defined by a e-beam lithography. (d) SiN front-side RIE and final membrane release: after developing the exposed resist, dry etching is again used to remove the exposed SiN areas; the membrane is released by wet etching in a KOH solution.

I) Back-side UV lithography.

The purpose of this first step is to define, on the back side of the sample, a specific pattern in an optical resist (as shown in Fig. 5.1a), so that the exposed regions can be subsequently etched. The sample initially consists of a 300 μm-thick chip of ⟨100⟩ Si, with a 300 nm layer of SiN on both the back and front side. To avoid contamination of the top surface, the chip is covered with a protective film of poly-methil-methacrylate (PMMA). This is obtained first by spin-coating the polymer (6000 rpm for 1 minute, AR-P679.04 950K PMMA) and then by baking the sample on a hot plate to evaporate the resist solvent (120°C for a minute).

Once the protective layer is deposited, an optical resist (S1818 by Shipley) is applied on the backside of the sample, using the same procedure and spin coater settings described above. After the baking step (90°C for a minute), the sample is transferred on the MJB4 mask aligner for the UV lithography. The sample is placed on the mobile stage and aligned, thanks to an optical microscope, with an exposure mask containing the pattern to impress on the resist. The UV lithography mask consists of a quartz plate with chrome patterns. Chrome is opaque to UV light while the remaining transparent areas form the desired pattern: light filters only through them when the mask is exposed to UV radiation and selectively exposes the optical resist on the sample, which is positioned immediately below the mask. The sample is brought in contact with the mask thanks to the mobile stage, and exposed for 3 s with UV light. Exposed resist regions are chemically modified by the radiation and, since S1818 is a positive resist, they can be removed by placing the sample in a beaker filled with a developer (MF319). After a 45 s development, the chip is rinsed with deionized (DI) water and blown dry with a N_2 flux.

The described protocol allows obtaining a resist mask on the backside of the sample that protects most of the chip surface, except for a set of $700 \times 700\,\mu\text{m}^2$ squares.

II) SiN back-side RIE and pre-etching.

The aim of this fabrication step is to etch the SiN on the back side regions not protected by optical resist and then to etch the bulk Si underneath by an anisotropic wet chemical attack. SiN regions not protected by the optical resist are removed by

a reactive ion etching (RIE) process (for details, see appendix): first of all the RIE chamber is cleaned for 3 minutes in Ar/O_2 plasma, to avoid contaminating the sample with residues from previous processes; the samples are then placed inside the chamber, backside up and etched for 5 minutes in a CF_4 (20 sccm) / H_2 (10 sccm) plasma, obtained by exciting the gas with 200 W RF power. The accurate selection of the process parameters, i.e. the gas flow rates and the RF power, is crucial to tune the relative importance of the physical and chemical components of the dry etch process and to achieve an etching with a vertical profile. At the end of the RIE step, the exposed SiN on the back side of the samples has been completely removed, as sketched in Fig. 5.1b.

The dry etching process of the SiN layer is followed by the wet etching of the Si underneath: a beaker filled with KOH:H_2O (1:2) is placed on a hot plate equipped with a thermometer and heated up to a temperature of 80°C; the sample is then mounted on a sample holder and placed into the beaker for 2 hours and 45 minutes. The KOH wet etching solution is strongly anisotropic on Si (about 1.5 μm/min in the $\langle 100 \rangle$ crystal direction) and strongly selective on SiN: this leads to the formation of a pit with a shape of a truncated pyramid with $\langle 111 \rangle$-oriented facets, as visible in Fig. 5.1b. The etch time was tuned to remove most of the Si, leaving only a residual layer approximately 30-50μ thick, immediately under the front side SiN. The sample is then extracted from the KOH solution and dipped twice in hot DI water for 30 s, to avoid the precipitation of KOH crystals on the sample. Finally, the chip is rinsed in isopropyl alcohol (IPA) and blown dry with a N_2 flux. The results of the wet etching process is shown in Fig. 5.1b.

III) Front-side EBL lithography.

The purpose of this step is to obtain, in the resist deposited on the front side of the sample, the patterns that will become through holes in the suspended SiN membranes. The sample is first cleaned in acetone and IPA, and baked at 150°C for a few minutes to minimize the impact of moisture on the surface. A double layer of the e-beam resist CSAR AR 6200 is then spin-coated on the front side of the sample: each deposition is obtained with the same procedure described at point I) for S1818, using this time 3000 rpm for 1 minute and 150°C as the spinning and baking parameters. Once the sample

has been covered in resist, it is placed in the EBL system. The machine coordinate system is accurately aligned with the edges of the Si chip, which are used as a reference so that the shapes of the holes can be impressed in the right position, i.e. in correspondence to the pits etched on the back side of the sample. Exposure is obtained using an electron beam energy of 30 keV and a dose per unit area of 400 μC/cm^2. After the exposure, the sample is removed from the EBL, placed on a beaker filled with developer AR 600-546 for 90 s, then rinsed in IPA for 30 s, in water for another 30s and finally baked for 1 minute at 150°C. A scheme of the process is shown in Fig. 5.1c.

IV) SiN front-side RIE and final etching.

The aim of this final step is to obtain free-standing SiN membranes with through holes of the desired geometry. After the usual preliminary chamber cleaning of 3 minutes, the sample is placed in the vacuum chamber and, as described in section II), the SiN is etched using the same plasma parameters used for the back side etching and a process time of 3 minutes. Once holes have been defined on the front side SiN, the residual $30 - 50\,\mu$m of Si has to be etched from underneath the SiN membrane. This is obtained following the same procedure for the wet etching described in point II). However, in this case, the exact immersion time in the KOH solution is established by observing the sample: when the membranes become transparent, the Si wet etching process has been completed. After removing the sample holder from the KOH and dipping it in hot DI water, the sample is carefully removed from the sample holder and rinsed in IPA, paying very close attention to hold it so that the membranes can be inserted vertically into the liquid. Such a procedure is necessary to minimize mechanical strain due to the liquid and to avoid breaking the membranes. For the same reason, the sample is then blown dry with a N_2 flux parallel to the surface. An example of one of the complete membranes is sketched in Fig. 5.1d and in the optical image of Fig. 5.2.

5.1.2 Graphene deposition

The final step of the sample preparation procedure is the transfer of monolayer graphene on the patterned SiN membranes. The flakes used for this thesis work have been grown

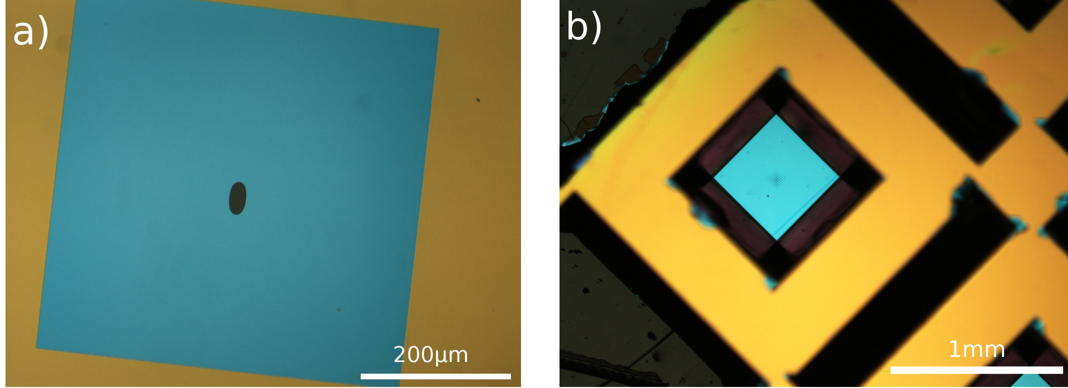

Figure 5.2: Optical images of a complete patterned SiN membrane. (a) Front side of the SiN suspended membrane (blue) with an elliptical through hole (black). (b) Back side of the chip: a pyramidal pit is digged into bulk Si (yellow-colored due to the SiN interference colors); the pyramid facets are visible as a black frame around the suspended SiN membrane (blue).

by chemical vapor deposition (CVD) on a copper substrate (see paragraph 2.2 for details about the growth procedure). In order to transfer CVD graphene from the Cu substrate to the SiN membranes, a 200nm-thick PMMA layer is spin coated on top of the Cu foil and used as a vector for the relocation of the flakes. The film can in fact be detached from the substrate through a process called "bubbling transfer": the Cu substrate is first inserted into a beaker filled with NaOH (1 M) solution and connected to the anode of a voltage generator, while the cathode is inserted in the liquid; by applying a tension of $2.3 - 2.5\,\text{V}$ between the electrodes, the H_2 bubbles induced by the water splitting reaction gently detach the PMMA and graphene from the substrate. The film, once completely separated from the copper, floats on the liquid and can be manipulated thanks to a plastic frame made of polyamide tape, which was previously applied to PMMA.

The polymeric vector is then attached to a custom support, which is designed to be compatible with the MJB4 mask aligner (see Fig. 5.3a). This allows to leverage on the precise mechanics system of the mask aligner and position the flakes to the target SiN membranes. When attaching the PMMA film to the alignment support, it is crucial to keep track of the side of the film with graphene and make sure it faces down towards the sample. In addition, it is extremely important to pay attention not to bend the film, since this can induce ripples and/or ruptures on the graphene flakes.

To complete the transfer, the SiN membranes prepared according with the proce-

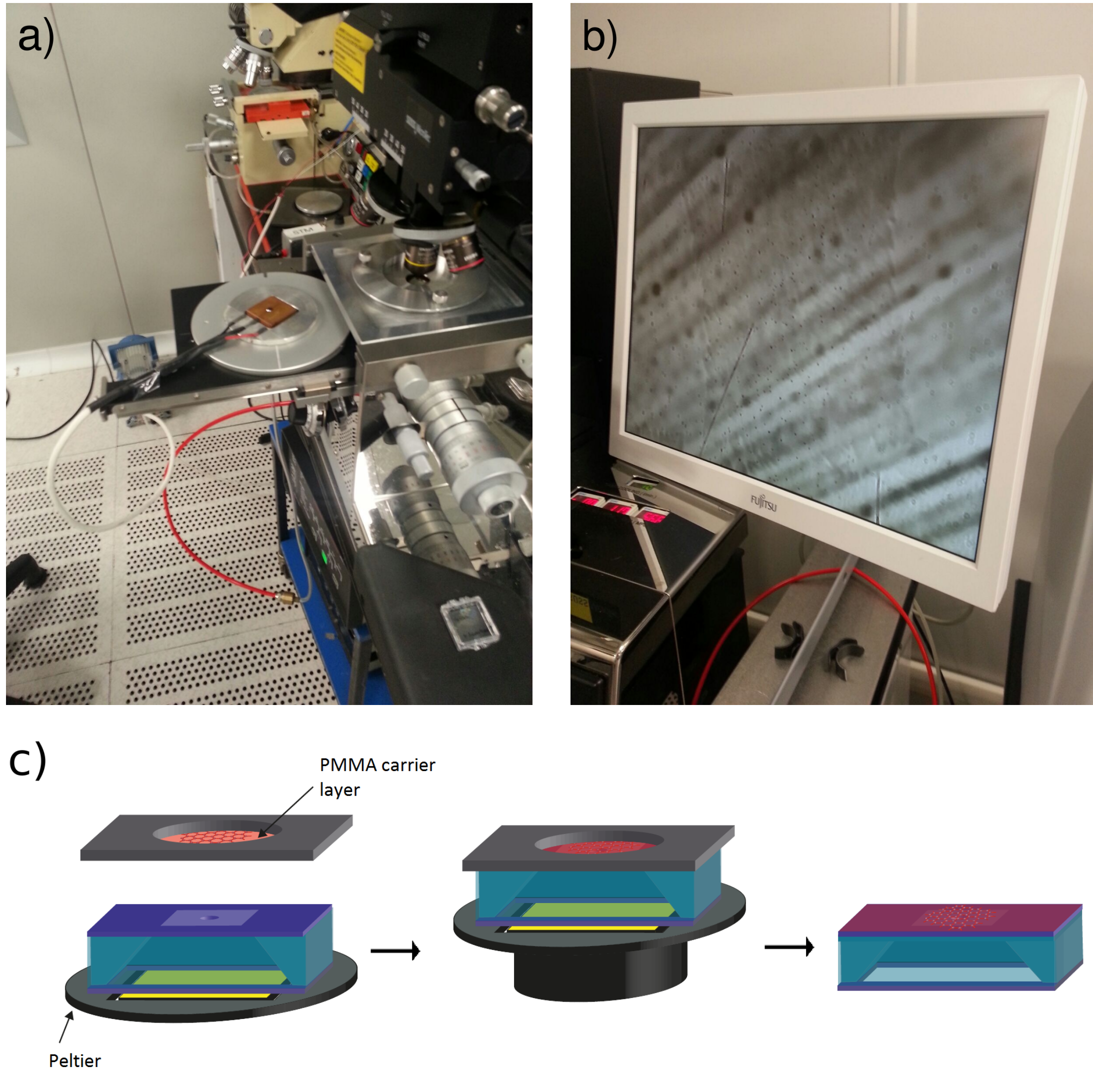

Figure 5.3: Experimental setup for graphene transfer. (a) Mask aligner adapter: the PMMA is positioned in the MJB4 mask aligner using a custom adapter (visible under the microscope objective); the sample is placed on a holder integrating a Peltier heater (in front of the microscope). (b) Optical image of a graphene flake on the PMMA film, as visible in the camera integrated in the MJB4 microscope. (c) Scheme of the transfer process: (i) the sample is placed on the Peltier mounted on the mobile stage; (ii) it is brought into contact with the PMMA carrier layer and the Peltier is then heated up to about 120°C, causing the PMMA to relax and to adhere to the membrane; (iii) once the sample is back to room temperature, the transfer is completed by cutting the PMMA film falling outside the Si chip.

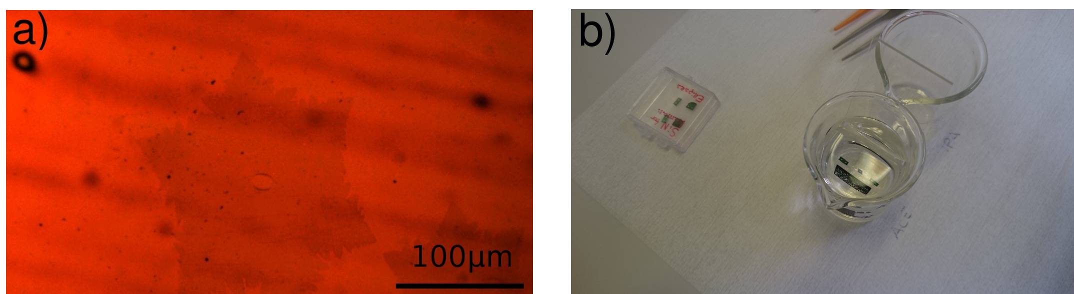

Figure 5.4: Images of the deposited flake and PMMA removal. (a) Optical image of one of the deposited graphene flake. A red filter was used to enhance graphene visibility. The elliptical hole in the SiN is visible at the center of the flake (dark red). Dark lines in the picture are due to fluctuation of the PMMA thickness related to the Cu large scale roughness. (b) The PMMA is removed in an acetone bath, using a beaker and a vertical glass support for the chips. Subsequently, the sample is placed in IPA and dried in N_2.

dure described in paragraph 5.1.1 are placed on a Peltier heater mounted on the mask aligner's mobile stage. After finding a suitable graphene flake with the optical microscope and aligning it on top of the hole in the SiN membrane, the mobile stage is raised until the film touches the sample (this can often be detected from the formation of an interference pattern due to multiple reflections between the sample surface and the polymeric film). The Peltier is then heated up to about 120°C, i.e. above the glass transition temperature of the PMMA. This causes the polymer to relax and to adhere to the SiN, together with the graphene flake. After turning off the Peltier and waiting for the sample to return to room temperature, the residual part of PMMA film outside the Si chip is cut away and the chip baked at 120°C to further promote the perfect adhesion between the PMMA and the sample. The deposition process is shown in Fig. 5.3c and an example of a complete device is shown in Fig. 5.4a.

The final step of the sample preparation is the removal of the PMMA layer. To this end, the sample is placed in a beaker with acetone for at least 30 minutes, rinsed in IPA for a minute and then blown dry with with a N_2 flux parallel to the surface. Due to the atomic thickness of monolayer graphene, it is necessary to insert/remove the sample very carefully in/from the liquids, and to maintain it vertical as much as possible (see Fig. 5.4b).

5.2 Description of the Raman setup

The experimental setup used to study the properties of strained graphene is shown in Fig. 5.5. A vacuum pump is connected, through a custom adapter, to a Tygon tube with an internal diameter of ≈ 0.5 mm and an outer diameter of 2.3 mm. The opposite end of the tube is attached to a small hollow metallic cylinder, which is soldered to a piece of stripboard with the same geometry of a standard microscope slide (see sketch in Fig. 5.6). A 2 mm-thick piece of elastomer (polydimethysiloxane, PDMS) is used as an adapter between the microtube and the sample: a through hole with the same size of the metallic cylinder is cut into the PDMS so that it can be placed on the stripboard and matched with the tube. The sample is placed on top of the PDMS, so that the SiN membrane is positioned in correspondence to the tube. Vacuum grease is used to minimize leaks due to the possible imperfect adhesion between the various material layers. The set-up allows to control the pressure of the bottom side of the SiN membrane, while its front side remains exposed to ambient pressure. The pressure differential plays the role of a vertical load to the SiN and graphene membranes and deforms them, thus generating the desired strain profile. In order to study the impact of strain on graphene, the stripboard is directly mounted on the stage of the Renishaw micro-Raman system, as visible in Fig. 5.5b.

After the vacuum pump is turned on, the pressure applied to the membrane can be regulated through a valve connecting the vacuum pump to the sample vacuum adapter, and measured using a vacuum gauge. The stability of the membrane load can be verified by measuring the pressure as a function of time in static vacuum conditions (i.e. with no direct pumping). Pressure is tipically found to decay over a time scale of more than one hour, ensuring that the reading on the vacuum gauge reliably corresponds to the actual pressure on the backside of the SiN membrane.

The absence of leaks is found to critically depend on the application of vacuum grease both on the top and on the bottom surface of the PDMS and the internal diameter of the tygon tube attached to the sample's support adapter. The microRaman system is used to study the deformed graphene samples by performing Raman spectroscopy (see Chapter 4). Measurements are performed using a solid-state laser emitting at a

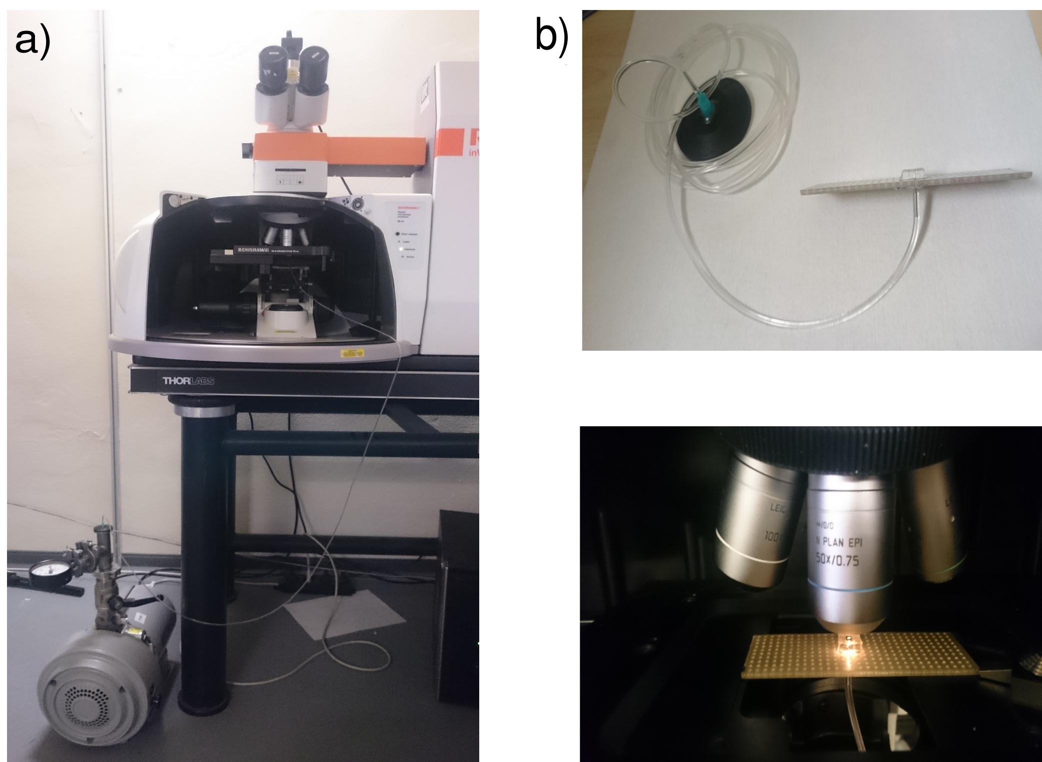

Figure 5.5: Experimental setup used for Raman measurements. (a) Overview of the Raman setup for the investigation of strain as a function of the membrane pressure load. (b) The sample holder, connected to the vacuum pump, has the same geometry of a microscope slide and allows an easy installation in the microRaman machine.

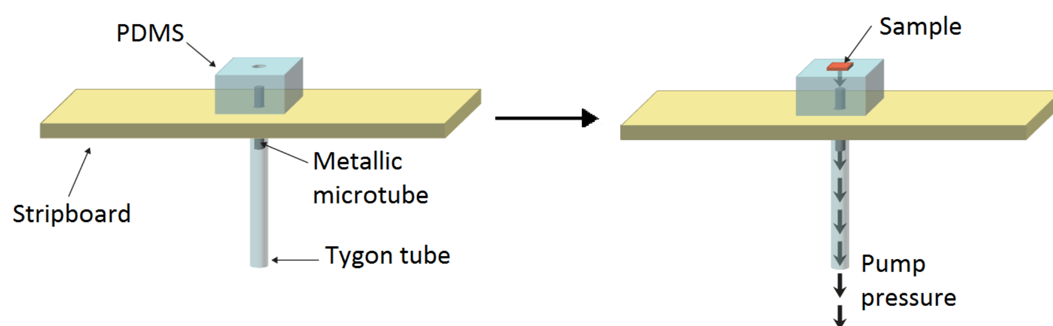

Figure 5.6: Scheme of the sample holder for the application of a pressure load to the graphene membrane.

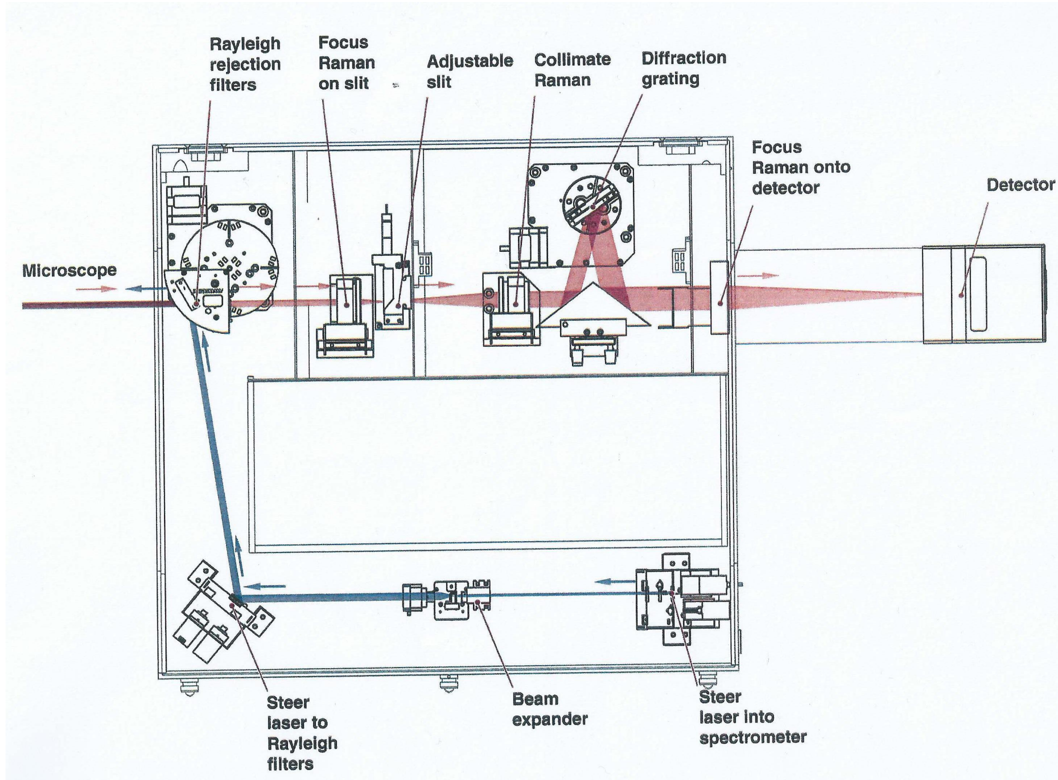

Figure 5.7: Scheme of the microRaman machine

wavelength $\lambda = 532\,\text{nm}$ with a maximum power of $100\,\text{mW}$ and a laser spot size of approximately $1\,\mu\text{m}$ in diameter [19]. The scattered light, collected through the same microscope, is then filtered with a dielectric edge filter, to reject the light generated from the Rayleigh scattering. The remaining Raman scattered light is then focused on a diffraction grating with 1800 lines/mm, in order to split it into its components, and directed towards a CCD. The system is connected to a computer that collects the data and elaborates them with the *WiRE* (Windows-based Raman Environment) software. A scheme of the microRaman equipment is shown in Fig. 5.7. After placing the sample holder on the microscope stage of the micro-Raman system and closing the stage door, the chip can be moved with a joystick and visualized thanks to the CCD connected to WiRE. The software allows selecting all the key parameters of the Raman measurement such as: the power of the laser light, the acquisition time and mode. Different measurement modes are in fact possible: in particular, in this thesis I used (i) single spectrum acquisitions and (ii) Raman maps. While the former results in a spectrum acquired by shining the laser on a single spot on the sample, the latter allows

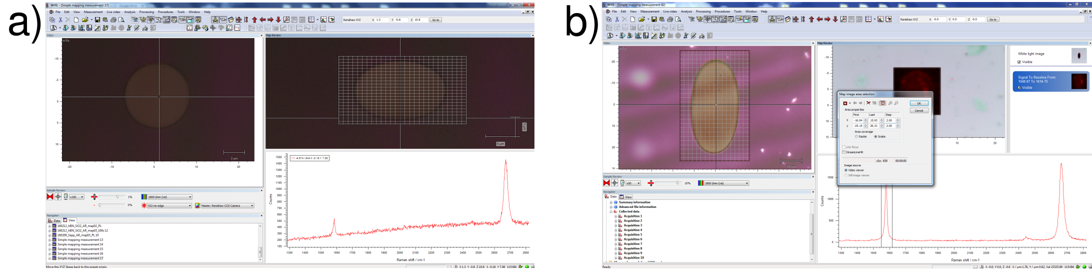

Figure 5.8: Screenshot of the WiRE software for micro-Raman acquisition, during (a) the acquisition of single spectra in custom positions of the membrane and (b) the definition of an acquisition grid for Raman maps.

designing an acquisition grid on the optical image of the sample and obtaining a full spectrum for each point of the grid.

WiRE stores the resulting spectra and provides a support for preliminary data analysis: for example, it allows obtaining an image of the signal intensity at a given wavelength and to fit the Raman spectra and display the map position or full width at half maximum (FWHM) of a specific Raman peak.

5.3 Raman spectroscopy on deformed graphene

5.3.1 Acquisition mode and parameters

The study of the effects of strain on suspended graphene is performed using the experimental setup described in the previous paragraph. The preparation process is the same for all the measurements performed during this thesis work: after placing the sample on the PDMS, paying attention to align it so that the interested membrane is directly on top of the hole, the support is mounted on the mobile stage. The joystick is used to position the sample under the microscope, until it appears on the software screen, as shown in Fig. 5.8a. The SiN hole is brought into focus by moving the mobile stage in the z direction, after having chosen the most appropriate objective (depending on the specific case, measurements were performed either using a 50X or 100X objective).

Once the sample is in position, the sample holder is connected to the vacuum pump through the adapter, as visible in Fig. 5.5a. The pump is turned on and the valve opened, so that a stable pressure is achieved: this leads to a differential pressure load applied to the suspended membrane, which causes it to bend (see Fig. 5.9).

Due to the large size of the SiN membrane and to the elastic response of PDMS, this slightly modifies the height of the sample, that needs to be compensated by a small refocusing. After readjusting the focus, the "map image acquisition" mode is selected, as visible in Fig. 5.8b. This allows obtaining detailed information on the properties of Raman peaks and their spatial variation on the suspended graphene. The acquisition grid is defined so to cover the whole free-standing graphene area and to collect between 350 and 500 pixels according to the size of the SiN hole, thus reaching a pixel size of about 1 μm. The power of the laser is set to 1% (corresponding to 1 mW) since a larger power can damage graphene and/or induce important heating effects, as suggested in [13] and [28]. The acquisition time is set to 5 s for each pixel, to improve the signal/noise ratio and obtain clean spectra. The acquired maps are then exported and elaborated with Matlab. Once the measurement process is completed, the pump is turned off and the pressure is reduced gently, to avoid damaging the free-standing graphene sample.

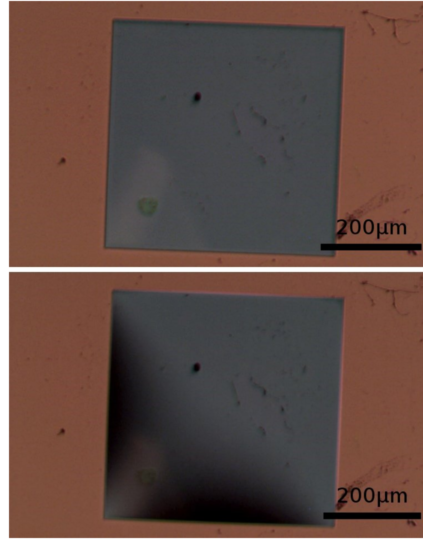

Figure 5.9: Optical image of a SiN membrane without and with the applied differential pressure.

5.3.2 Experimental results and interpretation

Data analysis

The experimental maps consist of matrices where each element is a full Raman spectrum. Data are collected at the positions defined by the acquisition grid, which can be drawn directly on top of the optical picture of the sample in the Renishaw system. Each Raman spectrum of monolayer graphene (see Chapter 4), presents two main peaks which are crucial to analyze the strain configuration of the material: the G peak, centered at about 1580 cm^{-1} and the $2D$ peak, centered at about 2680 cm^{-1}. A further D peak is observed in samples that contain a sizable amount of disorder but were typically absent in the studied samples: this indicates the lack of significant defects in the studied samples.

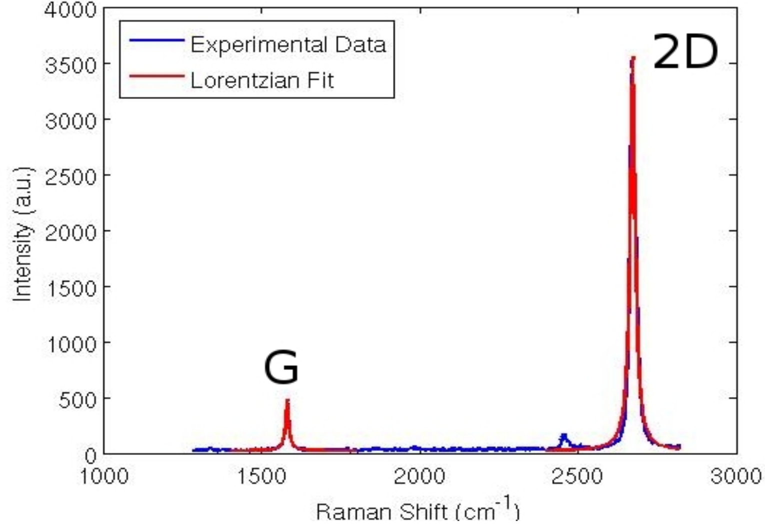

Figure 5.10: Example of Raman spectrum of suspended graphene with the lorentzian fit of its peaks.

Both peaks can be fitted using a lorentzian function

$$f(\Delta w) = \frac{a}{(\Delta w - b)^2 + c} + d, \tag{5.1}$$

where the variable Δw represents the wavelength of the Raman scattered light, measured in cm^{-1}, b is the center of the lorentzian peak and the parameter c is related to the FWHM Γ through the relation $\Gamma = 2\sqrt{c}$.

An example of a single Raman spectrum of monolayer graphene with the plot of the Lorentzian fit for the peaks $2D$ and G is shown in Fig. 5.10: the fit parameters, reported in the table below, were obtained using the non-linear fit Matlab function *nlinfit* and the lorentzian in equation (5.1).

	$2D$ peak	G peak
a (arb.units)	(4.2±0.2) $\times 10^5$	(2.4 ± 0.1) $\times 10^4$
b (cm^{-1})	2673.0±0.2	1581.6±0.2
c (cm^{-2})	119.2±6.6	52.5±3.0
d (arb.units)	22.9±10.8	28.1±1.2

The quality of the fit is proved by the high value of coefficient of determination R^2, equal to ≈ 0.99 for both peaks.

Simulation of the pressure-induced strain

Different strain profiles were realized using SiN membranes with holes of different geometries: elliptical and circular holes were used to induce and study uniaxial and biaxial strain, respectively. In the experiment, membranes are deformed by the application of a differential pressure, but the resulting strain cannot be directly measured. For this reason, strain for a given pressure load ΔP was simulated using COMSOL, a commercial finite element solver for partial differential equations in general, and mechanical problems in particular. The software allows to create a 3D model of suspended graphene and to simulate its response to mechanical stress. To this end, known mechanical properties of graphene (Young's modulus $E = 1\,\text{TPa}$ and Poisson ratio $\nu = 0.165$, see Ref.[37]) were provided as an input and the simulation was run for different values of the pressure applied to the top and bottom surfaces of the graphene membrane.

From the numerical results, it is possible to predict the mechanical response of the system, such as the stress and strain tensor and the vertical displacement of the membrane. As shown in Fig. 5.11a and Fig. 5.11b, several simulations were performed while changing the value of the pressure load, in order to study its influence on the

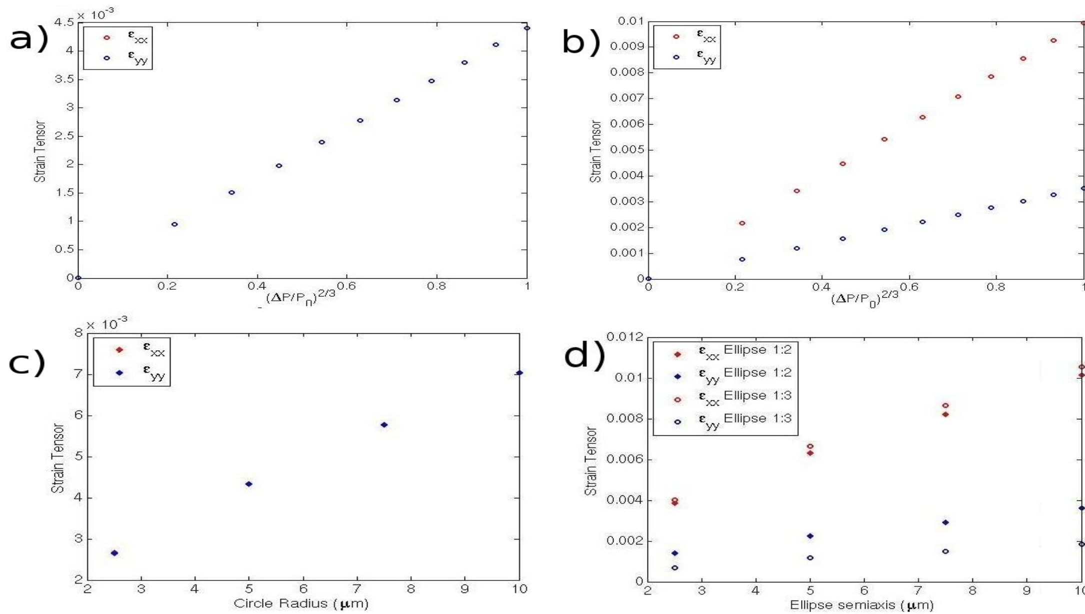

Figure 5.11: Simulated values of the strain tensor elements ϵ_{xx} and ϵ_{yy} at the center of the membrane as a function of the pressure load ΔP, for a circular hole of $10\,\mu$m diameter (a) and an elliptical hole of major and minor axis of 40 and $20\,\mu$m (b), and of the size of the SiN hole, for both a circular (c) and 1×2 and 1×3 elliptical geometries (d) in the presence of a 1 bar pressure load.

strain. The results indicate that, for circular holes, the values of the strain tensor elements ϵ_{xx} and ϵ_{yy} at the center of the membrane remain equal, thus creating a biaxial strain region. Differently, for the elliptical holes, the values of the strain tensor is strongly non isotropic, as visible from the different values of ϵ_{xx} and ϵ_{yy}. In both cases the strain was found to scale as $\Delta P^{2/3}$, as expected [38].

Further simulations were performed to study the relation between the value of ϵ_{xx} and ϵ_{yy} and the dimensions of the hole in the suspended membrane where the graphene is deposited, under the application of a differential pressure of 1 bar. For the simulation circles and ellipses with a proportion 1:2 and 1:3 between minor and major axis were taken into consideration. The results, shown in Fig. 5.11c and 5.11d, indicate that for all the shapes the magnitude of the strain at a given pressure load ΔP increases with the dimension of the hole and, in the case of elliptical holes, so does the difference between ϵ_{xx} and ϵ_{yy}.

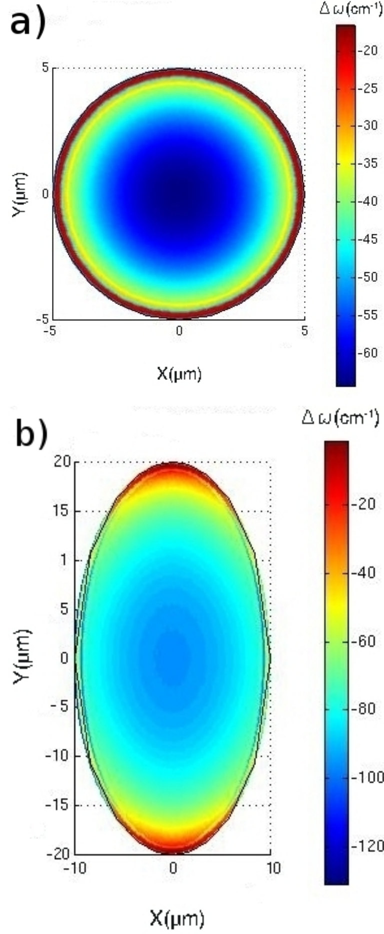

Figure 5.12: Expected strain-induced $2D$ peak shift profiles in graphene on pressure-loaded membranes with a circular (a) and an elliptical (b) hole.

Using the formulas and the parameters reported in [13] and [28], it has also been possible to simulate the profile of the peak shift for small strain. For example, based on values of the Grüneisen parameters available in the literature, the $2D$ peak is expected to display the shift reported in Fig. 5.12a and Fig. 5.12b, according to the equation

$$\Delta\omega_{2D} = -\omega_{2D}^{0}\gamma_{2D}(\epsilon_{xx} + \epsilon_{yy}) \tag{5.2}$$

where ω_{2D}^{0} is the frequency of the peak position at zero strain, γ_{2D} is the Grüneisen parameter for the $2D$ peak and ϵ_{xx} and ϵ_{yy} are the diagonal elements of the strain tensor.

Experimental results

Every spectrum contained in the Raman data is analyzed by fitting the G and $2D$ peak with the lorentzian function (5.1). The various fit parameters can be used to generate new maps illustrating their variation over the scanned area. Fits performed as a function of the applied pressure yield useful information about the effect of strain on graphene and about its dependence on the shape and dimension of the holes and on other relevant factors. In order to study the graphene response to the strain, several maps were acquired with the procedure described in the previous subsection and elaborated with Matlab. In the beginning, maps were acquired for devices where the PMMA carrier layer was not removed. In fact, the suspended graphene layer becomes much more fragile after the PMMA removal: for this reason, maps on real free-standing graphene were only performed in a second step.

A. Mapping of the strain in PMMA-covered graphene samples

The first striking effect of the strain in suspended graphene, as anticipated in Chapter 4, is the evident redshift in the position of the peaks. This is shown for a single spectrum in Fig. 5.13, referring to an elliptical membrane with major and minor axis of 10 and 5 μm for $\Delta P = 0$ (blue curve) and in the presence of a load $\Delta P = 1$ bar (red curve), respectively. A similar effect occurs for every point of the suspended membrane

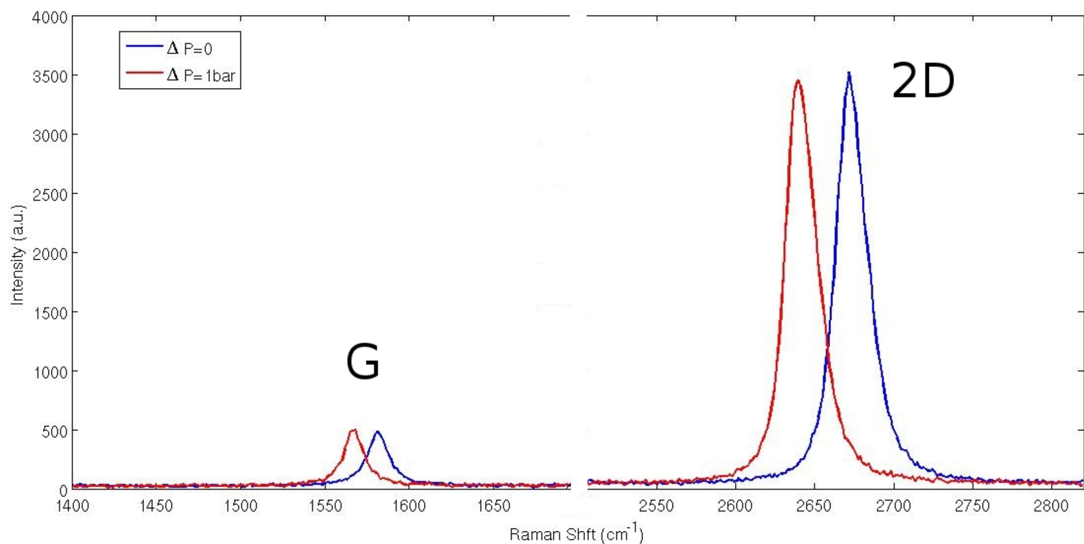

Figure 5.13: Example of the red shift of the Raman G and $2D$ peaks in graphene, when a pressure difference of 1 bar is applied to the suspended membrane.

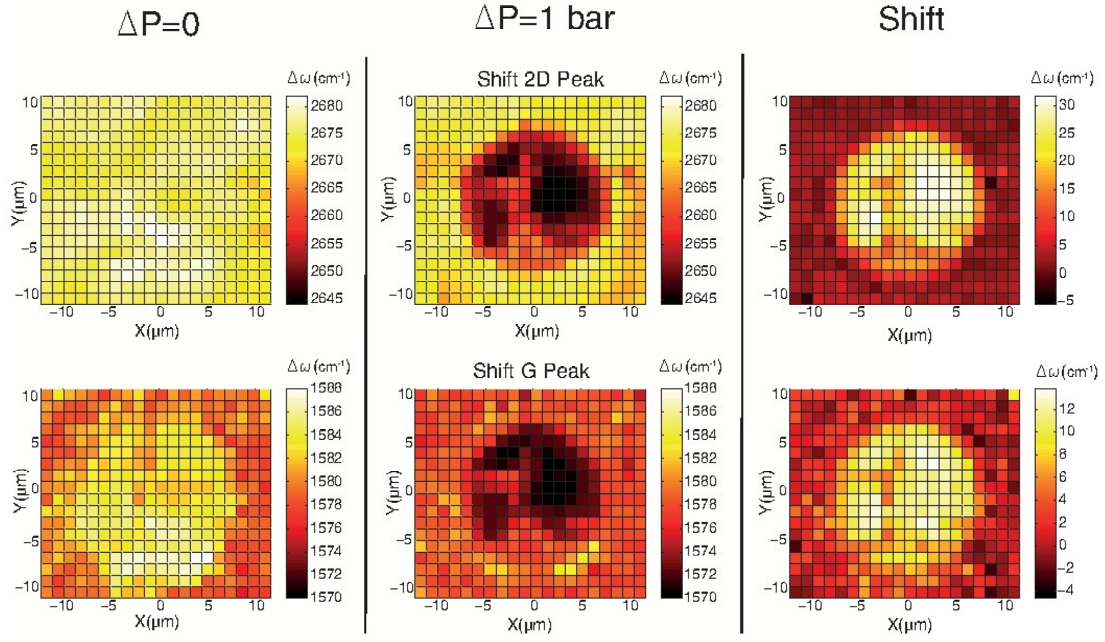

Figure 5.14: Pressure-induced shift of the Raman peaks. Maps depict the position of the $2D$ (first row in each panel) and G (second row in each panel) Raman peaks. Spectra were collected for graphene suspended on a circular hole with a diameter of $15\,\mu$m, before the removal of the PMMA carrier layer.

and can be used to map the shift of the G and $2D$ peaks. For instance, the first column of Fig. 5.14 shows the maps for the $2D$ and G peak positions obtained at $\Delta P = 0$ for a circular membrane: the uniform value of peak positions (around $2680\,\mathrm{cm}^{-1}$ for the $2D$ peak and $1580\,\mathrm{cm}^{-1}$ for the G peak) suggests that in the sample there is no initial strain profile in the suspended graphene. The slight difference between the peak position inside and outside the hole is due to the interaction with the SiN and/or to a uniform pre-stress due to the adhesion of graphene on the vertical walls of the SiN hole [37]. The second column shows the position of the peaks in the presence of a $\Delta P = 1\,\mathrm{bar}$ pressure load: the $2D$ peak (first row) shifts to $2645\,\mathrm{cm}^{-1}$ at the center of the circular hole. At the same time, the G peak reaches, in the region of maximum shift, $1570\,\mathrm{cm}^{-1}$. The third column displays the map of the relative shift for both peaks, obtained as the difference between the maps in the first and the second column: the shift profile thus obtained is non-uniform and it is generally in good agreement with what expected from simulations (see Fig 5.12). On the other hand, important irregular features are also visible in the shift map: as shown in measurements discussed further

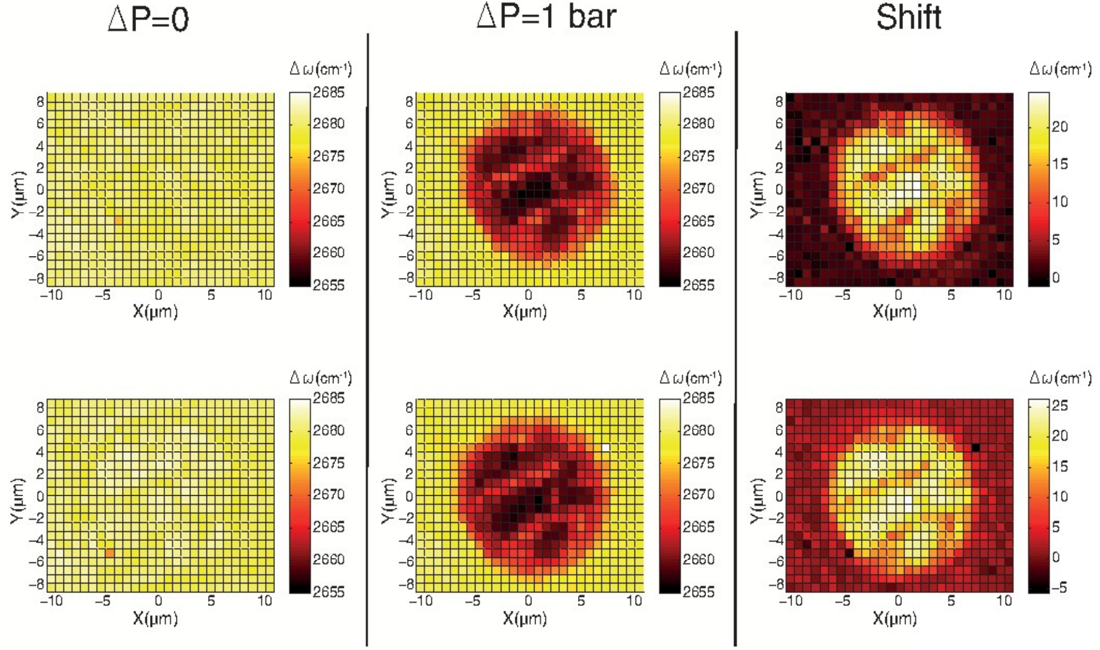

Figure 5.15: Reproducibility of the loading procedure. The panel displays repeated maps of the position of the $2D$ peak for suspended graphene, before the removal of the PMMA carrier layer. All maps were acquired using a circular SiN hole with a diameter of $15\,\mu$m. Consecutive measurements were performed at $\Delta P = 0$ (first row, first column), $\Delta P = 1\,$bar (first row, second column), and then again at $\Delta P = 0$ (second row, first column), $\Delta P = 1\,$bar (second row, second column). The corresponding peak shift is reported in the third column.

on, these are related to the mechanical effect of the PMMA carrier layer.

Before proceeding in a deeper analysis of the Raman maps, a critical aspect of the experiment that needs to be addressed is the adhesion between graphene and the supporting SiN membrane. Graphene's clamping is in fact crucial for the correct operation of the set-up and for the comparison between experimental data and simulations. The stability of the flake boundary conditions was verified by acquiring multiple maps, alternating configurations with $\Delta P = 0$ and with $\Delta P = 1\,$bar: in the absence of graphene slipping, Raman peaks in fact have to recover their initial position after the removal of the pressure load. This kind of tests were regularly performed on all the studied graphene membranes. A specific example is reported in Fig. 5.15 and refers to the $2D$ peak in a circular membrane. Maps were acquired by applying, in sequence: zero strain (first column, first row); maximum strain (second column, first row); zero strain (first column, second row); maximum strain (second column, second row). The third column

shows on both rows the relative shift of the peak as a function of the position, which is calculated as a difference between the map at $\Delta P = 1\,\text{bar}$ and the one at $\Delta P = 0$. As visible in the first column, the map of peak positions for unstrained graphene does not display a significant variation, regardless of the membrane history in terms of pressure load: the $2D$ peak in both maps is centered uniformly at around $2680\,\text{cm}^{-1}$. The absence of variations, combined with the reproducibility of the strain profile at $\Delta P = 1\,\text{bar}$ in the second column, indicates that the graphene is stably attached to the SiN and no slipping occurs during the loading.

B. Mapping of the strain in PMMA-free graphene samples

The same experiments were later performed also on samples where the PMMA carrier layer was completely removed. In this case membranes were found to be significantly more fragile: not all the membranes survived to the application of $\Delta P = 1\,\text{bar}$, most likely because of small defects or rupture over the hundreds of square microns of suspended graphene. Results in Fig. 5.16 indicate that, for both the $2D$ peak (first row) and the G peak (second row), the position of the Raman peak in the absence of a pressure load is not sensitive to the membrane history (in particular to the application of a pressure load of 1 bar). Each row in the figure contains maps obtained in the load sequence $\Delta P = 0$ (first column), $\Delta P = 1\,\text{bar}$ (second column) and, again, $\Delta P = 0$ (third column). At $\Delta P = 0$, peaks are reproducibly found to occur at $2680\,\text{cm}^{-1}$ and $1585\,\text{cm}^{-1}$ for the $2D$ and G Raman modes, respectively. This confirms that clamping of graphene is not simply caused by the PMMA layer but it is rather present because of the direct adhesion on the SiN, as a consequence of Van der Waals interaction.

Despite their fragility, graphene membranes free from PMMA are crucial to investigate the impact of strain on graphene. PMMA in fact strongly modifies the mechanical response of the suspended part of the device. This is demonstrated in Fig. 5.17, where two samples were compared: both consisted of graphene deposited on an elliptical hole of dimensions $20\,\mu\text{m} \times 40\,\mu\text{m}$; one was still covered by the PMMA carrier layer while the other one had no PMMA. As in previous figures, the first column refers to the $\Delta P = 0$ configuration, the second one to $\Delta P =$ 1bar and the third one to the shift, obtained as a difference of the two maps. Raman peaks at zero strain is very similar for the two samples. Differently, in the presence of a pressure load of 1 bar, the redshift of the peaks

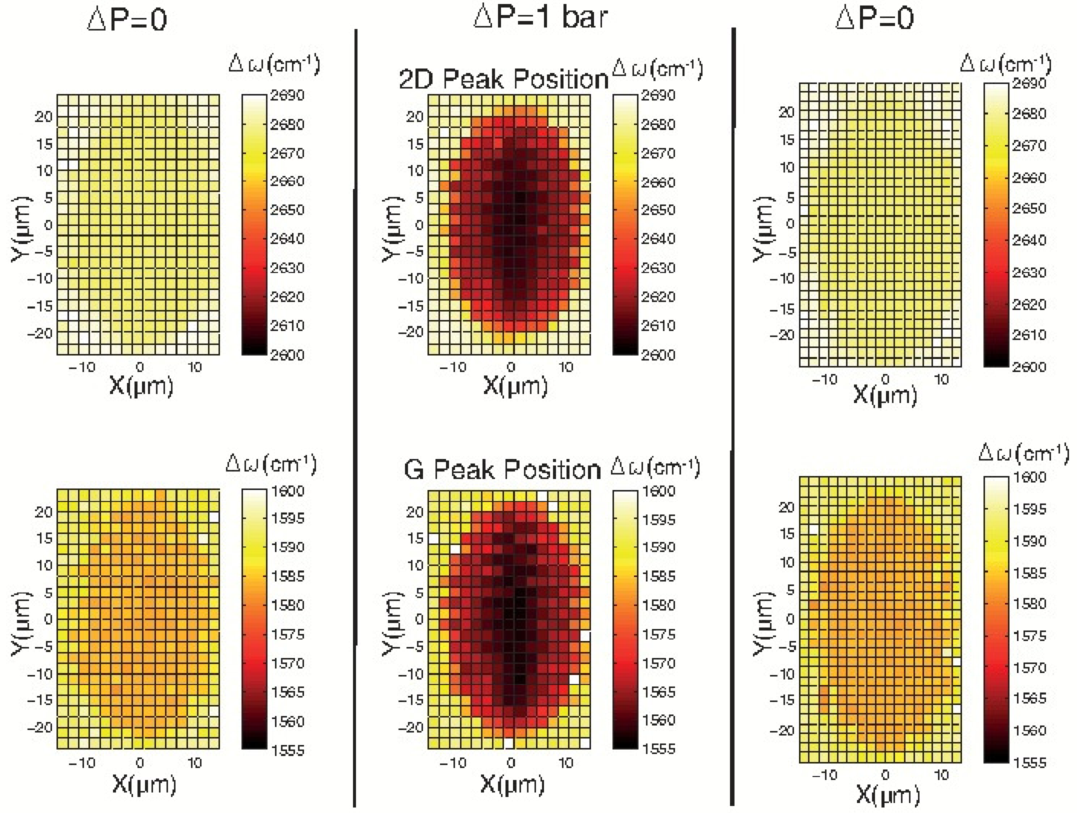

Figure 5.16: Reproducibilty of the loading procedure for graphene membranes without PMMA. Maps of the $2D$ and G peak positions for suspended graphene on an elliptical SiN hole with minor and major axes of 20 and 40 μm. Data were sequentially acquired for $\Delta P = 0$ (first column), $\Delta P = 1$ bar (second column) and again $\Delta P = 0$ (third column).

is significantly larger on the sample without the PMMA carrier layer. In fact, focusing on the second column of Fig. 5.17a, it is possible to notice that the $2D$ peak, starting from an initial position at around 2680 cm^{-1}, reaches about 2650 cm^{-1}; differently, in Fig. 5.17b the position of the peak in the areas of maximum strain is about 2600 cm^{-1}. A comparable difference in the magnitude of the measured peak shift can be observed for the G peak, that, starting from an initial position at 1580 cm^{-1}, shifts to 1573 cm^{-1} in the sample with the PMMA and 1555 cm^{-1} in the sample without it. This is also clearly visible in the shift maps reported in the third column: the maximum shift values of 32 cm^{-1} and 10 cm^{-1} for the $2D$ and G peak in the sample with the PMMA increases to 70 cm^{-1} and 27 cm^{-1} in the sample where PMMA was removed.

The different observed shifts can be easily explained based on the elastic response of the PMMA. Since there is no significant variation in the Raman spectra between

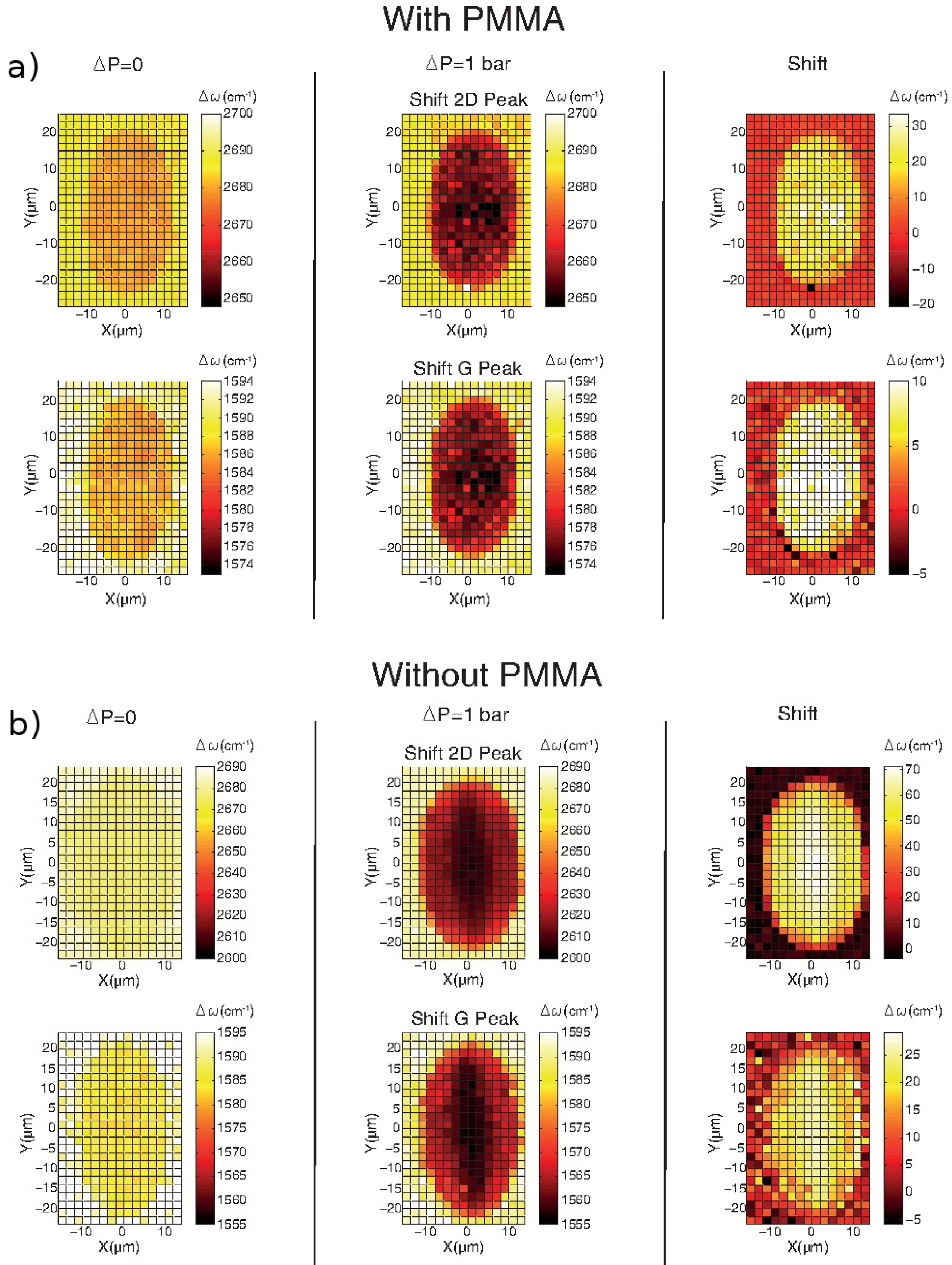

Figure 5.17: Maps of $2D$ (first row in each panel) and G (second row in each panel) Raman peaks of suspended graphene with the PMMA carrier layer (a) and without it (b) on an elliptical hole of minor and major axes 20 and 40 μm, before applying the pressure difference (first column), after (second column) and the peak shift given by their difference (third column).

the two samples in the absence of a pressure load, it is reasonable to conclude that the presence of the PMMA layer (about 200 nm-thick) over the entire sample affects only the mechanical properties of the membrane and does not induce any further shift due, for instance, to doping or other kind of interactions between the two materials. The impact on the mechanical properties can be estimated in terms of the two-dimensional Young modulus E_{2D} of the compund membrane including graphene *and* PMMA. For a single-layer material $E_{2D} = \tau E$, where τ is the thickness of the layer. Differently, for a double layer $E_{2D} = E_1\tau_1 + E_2\tau_2$, giving rise to a compound mechanical response of graphene and PMMA. The polymeric layer has a much smaller value of E (few GPa), but its thickness is almost one thousand times larger than the one of graphene. As a result, the presence of the PMMA has a measurable impact over the total E_{2D} of the membrane and thus on the value of the strain and of the observed Raman shifts. In addition, it is worth noting that the PMMA carrier layer has not generally a uniform thickness because of the residual roughness of the Cu growth substrate. This leads to an artificial inhomogeneity in the mechanical response of the membrane, which is for instance well visible in Fig. 5.15. In the following, the quantitative analysis of the shift of the peak positions will exclusively focus on the case of membranes free of the PMMA carrier layer. In fact, only in this case the shift can be directly compared with the strain profiles that can be calculated numerically.

C. Strain tuning as a function of the pressure load

The central important feature of the investigated SiN devices is that they allow tuning the magnitude of the strain. In the limit of small deformations, strain is expected to scale as $\Delta P^{2/3}$, as argued in the literature [38] and confirmed by numerical simulations reported in the previous sections. As a consequence of equation (5.2), the position of the Raman peaks is also expected to scale linearly with $\Delta P^{2/3}$. Tunability was explored on the $20\,\mu$m $\times$ $40\,\mu$m elliptical membrane of Fig. 5.17b, on circular membranes with a diameter of $10\,\mu$m and on elliptical ones $5\,\mu$m $\times$ $10\,\mu$m. A series of measurements were realized by acquiring a single spectrum at the center of the SiN holes, where the maximum average strain is expected to occur according to simulations shown in Fig. 5.12. Data were collected as a function of the pressure of the pump and thus of the differential load ΔP applied to the membrane.

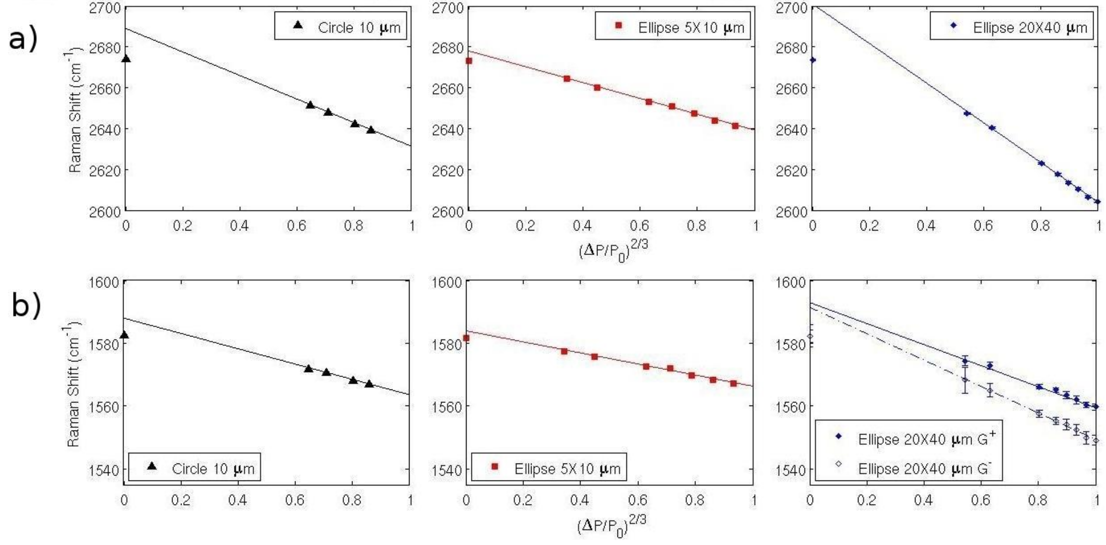

Figure 5.18: Position of the $2D$ peak (a) and G peak (b) varying the differential pressure applied on a membrane with a cirluclar hole of 10 μm diameter (fist column), an elliptical hole of dimensions 5x10 μm(second column) and an elliptical hole of dimensions 20x40 μm (third column).

The positions of the Raman peaks was obtained using a lorentzian fit function and are plotted as a function of the adimensional parameter $\eta = (\Delta P/P_0)^{2/3}$, with $P_0 = 1$bar, in Fig. 5.18a ($2D$ peak position) and Fig. 5.18b (G peak position). Raw data are reported in the appendix. The plots indicate that, as expected, the dependence of the position of the peaks is linear in $\Delta P^{2/3}$ and clearly demonstrate that the strain can be controlled by the applied differential pressure. The linear fit of the peak position is directly related to the Grüneisen parameters for graphene and yields the parameters listed in Tab. 5.1. It should be noted that, while most of the datapoints in Fig. 5.18b nicely fall on a line, the peak position at $\Delta P = 0$ clearly displays a further red shift. This behavior is likely caused by graphene adhesion on the SiN vertical wall, which creates a tensile strain even at zero load. The effect is expected to become negligible at finite pressure load and all linear fits were performed excluding the Raman shift value at $\Delta P = 0$. Similar deviations have been consistently observed in circular inflated graphene bubbles, but a conclusive demonstration of their origin is still missing at the moment.

The experimental results are in good agreement with theoretical prediction. In order to see this, as explained in Chapter 4, the slopes in Fig. 5.18a and Fig. 5.18b have been used to calculate the corresponding Grüneisen parameters for the various Raman peaks

in graphene. Calculations were in this case based on the simulated strain as a function of η, for the same membrane geometry of the measured devices. We recall that the $2D$ and G peak shifts are related to strain by

$$\Delta\omega_{2D} = -\omega_{2D}^0\gamma_{2D}(\epsilon_{xx} + \epsilon_{yy}) = -2\omega_{2D}^0\gamma_{2D}\bar{\epsilon} \tag{5.3}$$

$$\begin{aligned}\Delta\omega_{G^\pm} &= -\omega_G^0\gamma_G(\epsilon_{xx} + \epsilon_{yy}) \pm \frac{1}{2}\beta_G\omega_G^0\sqrt{(\epsilon_{xx} - \epsilon_{yy})^2 + 4\epsilon_{xy}} \\ &= -2\omega_G^0\gamma_G\bar{\epsilon} \pm \frac{1}{2}\beta_G\omega_G^0\Delta\epsilon.\end{aligned} \tag{5.4}$$

In the case of the $2D$ peak, a simple redshift is expected regardless of the exact nature of the strain profile and data in Fig. 5.18a confirm this expectation. Differently, anisotropic strain $\Delta\epsilon = \sqrt{(\epsilon_{xx} - \epsilon_{yy})^2 + 4\epsilon_{xy}}$ is known to cause the doubly degenerate G peak to linearly split in the G^+ and G^- peaks, while the hydrostatic component $\bar{\epsilon} = (\epsilon_{xx} + \epsilon_{yy})/2$ is responsible for the general redshift of both peaks. However, based on the known value of β_G and on the simulations in Fig. 5.11a and Fig. 5.11d, the second term of equation (5.4) is not expected to be observable, neither for circular nor for small elliptical holes. In fact, ϵ_{xx} and ϵ_{yy} are equal in the former case, while their difference can be so small that the contribution of the second term to the total shift is hard to detect in the latter case. On the other hand, the maximum strain anisotropy increases with the dimensions of the ellipse, and indeed a splitting of the G peak could be observed on graphene suspended on the biggest SiN ellipse studied, i.e. on the one with axes 20 and 40 μm. In fact, the analysis of the Raman map acquired over the sample with ΔP = 1bar shows not only the peaks shift displayed in Fig. 5.17b, but also a non-trivial evolution of the peak width, as shown in Fig. 5.19a. It demonstrates clearly the presence of the anisotropic strain, whose profile is in good agreement with what expected from the simulations (see Fig. 5.19b). In this case, instead of fitting the G peak with a single lorentzian curve, the sum of two lorentzian functions has been used, both with a peak width fixed to the value obtained for $\Delta P = 0$. While the general redshift of the G peaks is clearly visible in Fig. 5.18b, this procedure allowed to track the two peak components in the panel referring to the large elliptical SiN hole (plot

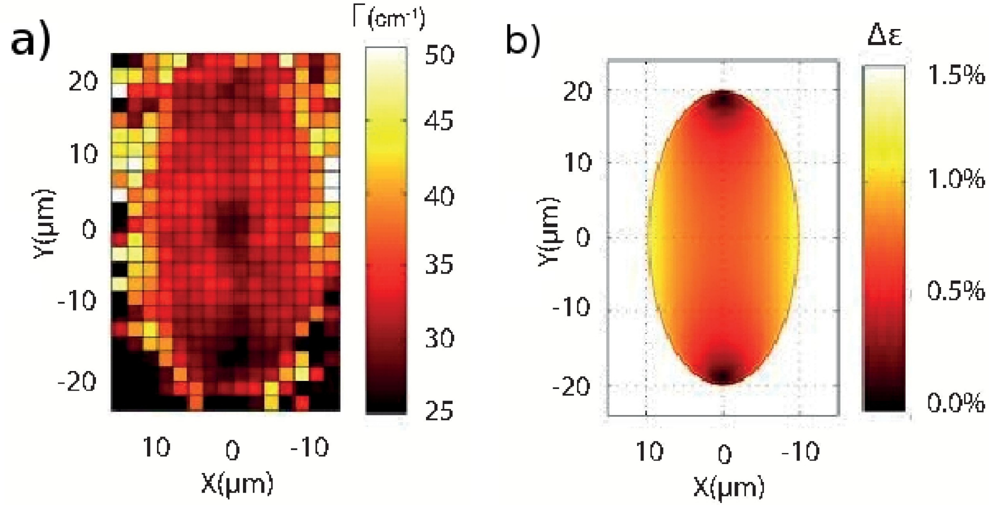

Figure 5.19: Anisotropy and broadening of the Raman G peak. (a) Map of the G peak width Γ for graphene suspended on an elliptical hole of minor and major axes 20 and 40 μm with an applied pressure load of $\Delta P = 1$bar, obtained by fitting the peak with a single Lorentian curve, and (b) the strain anisotropy map obtained from the simulation of the same geometry at $\Delta P = 1$bar.

on the bottom-right end of the figure). The results obtained for the position of these peaks are replotted for clarity in Fig. 5.20, along with an example of a double peak fit of a dataset displaying a lineshape that clearly deviates from a single lorentzian. The resulting peak positions indicate a splitting which is again linear in $\Delta P^{2/3}$ and thus in the strain parameters, as expected.

From the fit parameters reported in Table 5.1a, 5.1b, it has been possible to estimate the experimental trends of the peak shift as a function of the strain, as obtained from the simulations for the different studied geometries, in the presence of an applied pressure load $\Delta P = 1$bar. The results, along with the simulated strain values, are reported in Table 5.1c and are compatible with recent works on strained graphene [12, 13]. Starting from these values, the experimental Grüneisen parameter γ can be estimated using the formulas

$$\gamma_{2D/G} = \frac{1}{2\,\bar{\epsilon}\,\omega^0_{2D/G}} \cdot \frac{\partial \omega_{2D/G}}{\partial \eta} \tag{5.5}$$

where $\partial \omega_{2D/G}/\partial \eta$ is the slope of the experimental linear fit, $\omega^0_{2D/G}$ is the value of its intercept at $\Delta P = 0$ and $\bar{\epsilon}$ is the hydrostatic strain value obtained from the simulation and reported, for each geometry, in Table 5.1c. A factor 100 must be used if strain is measured in percent units. In the case of the biggest measured ellipse, starting from

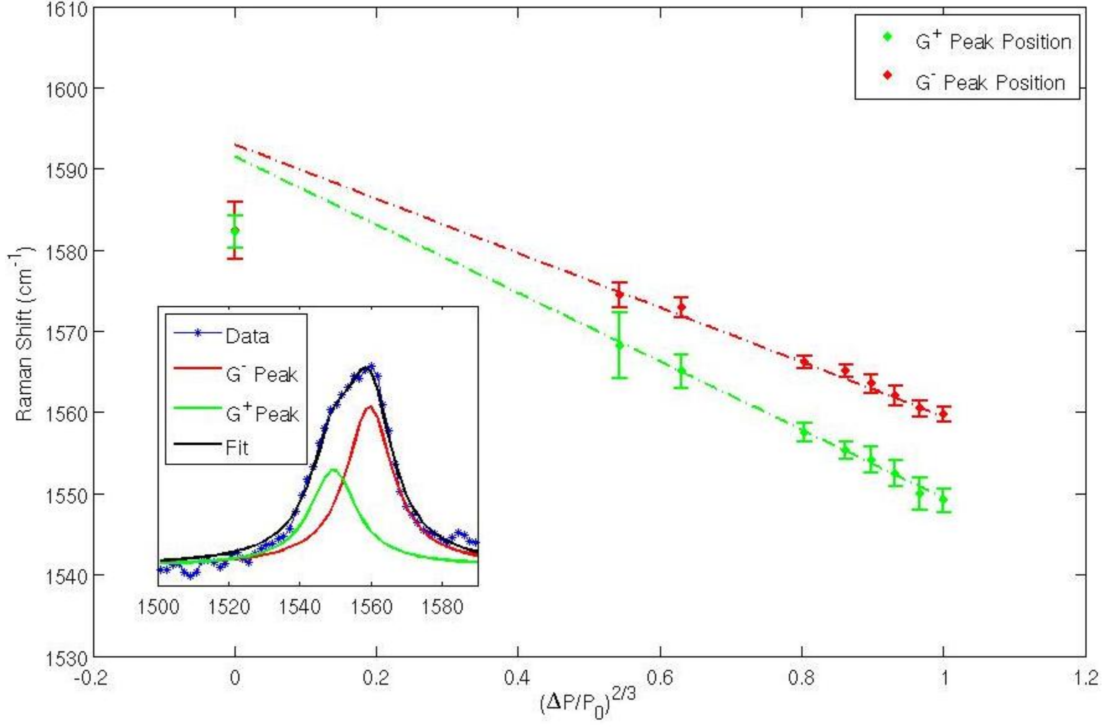

Figure 5.20: Plot of the position of the center of the two lorentzian peaks used to fit the G peak for a sample of graphene deposited on an elliptical hole.

	$\partial\omega_{2D}/\partial\eta$	ω^0_{2D}
Circle 10 μm	-57.0±9.0	2688±7
Ellipse 5x10 μm	-38.7±2.3	2678±2
Ellipse 20x40 μm	-97.7±2.9	2701±2

(a)

	$\partial\omega_G/\partial\eta$	ω^0_G
Circle 10 μm	-23.4±6.5	1587±5
Ellipse 5x10 μm	-17.6±1.8	1584±2
Ellipse 20x40 μm G^+	-33.5±3.2	1593±3
Ellipse 20x40 μm G^-	-42.0±2.4	1591±2

(b)

	$\bar{\epsilon}$ (%)	$\Delta\epsilon$ (%)	$\partial\omega_{2D}/\partial\bar{\epsilon}\,(\mathrm{cm}^{-1}/\%)$	$\partial\omega_G/\partial\bar{\epsilon}\,(\mathrm{cm}^{-1}/\%)$
Circle 10 μm	0.44		-130	-53
Ellipse 5x10 μm	0.26		-143	-65
Ellipse 20x40 μm	0.67	0.64	-144	-50(G^+) -63(G^-)

(c)

Table 5.1: Tables of the results of the linear fit of the $2D$ (a) and G (b) peak position for every simulated geometry, the numerical estimate of the maximum strain for a pressure load of 1bar, according to the simulations, and the calculated trends of the peak shift as a function of the strain (c).

	γ_{2D}	γ_G	β_G
Circle 10 μm	2.41±0.39	1.68±0.47	
Ellipse 5x10 μm	2.67±0.15	2.05±0.21	
Ellipse 20x40 μm	2.67±0.08	1.77±0.27	0.84±0.13

Table 5.2: Table of experimental Grüneisen parameters.

	γ_{2D}	γ_G	β_G
Ref [14] for biaxial strain	2.6±5%	1.8±10%	
Ref [13] for uniaxial strain	3.55	1.99	0.99
Ref [13] for uniaxial strain (theorical)	2.7	1.87	0.92
Ref [12] for uniaxial strain (theorical)		1.86	0.96

Table 5.3: Table of Grüneisen parameters reported in the literature.

formula (5.4), the following equation for the Grüneisen parameter γ_G and the shear deformation potential β_G have been used

$$\gamma_G = \frac{1}{4\,\bar{\epsilon}\,\omega_G^0}\left(\frac{\partial\omega_{G^+}}{\partial\eta} + \frac{\partial\omega_{G^-}}{\partial\eta}\right) \tag{5.6}$$

$$\beta_G = \frac{1}{4\,\Delta\epsilon\,\omega_G^0}\left(\frac{\partial\omega_{G^+}}{\partial\eta} - \frac{\partial\omega_{G^-}}{\partial\eta}\right). \tag{5.7}$$

The estimated Grüneisen parameters have been summarized in Tab. 5.2, along with their respective errors, calculated based on the fit errors and on the uncertainty over the pressure value, equal to 40mbar. The value of these adimensional parameters is in remarkably good agreement with those reported in the literature [12–14], which have been summarized in Tab. 5.3.

In conclusion, the discussed experimental results demonstrate a novel way to obtain and control non-trivial strain profiles in suspended graphene. While circular membranes have been explored in the past, the present work on elliptical clamping geometries provides a first demonstration that non-isotropic strain profiles can be obtained once suitable SiN structures are designed. This strategy can in principle be extended further and even used to induce the peculiar non-uniform strain profiles giving rise to pseudomagnetic effects in the honeycomb lattice of graphene.

Active devices for strain engineering

In order to achieve and control pseudo-magnetic fields in graphene, and thus induce a tunable quantization of the electronic states, it is fundamental to conceive new ways to actively tune the strain in graphene. Beside the devices described in the previous chapter, that exploit a differential pressure to control the strain, further methods to engineer the strain on graphene have been preliminary investigated during the thesis project. These involve the use of electrostatic forces to actively deform the mechanical structure onto which graphene is clamped, allowing the creation of tunable strain devices.

6.1 Design of SiN membranes with comb actuators

The first alternative method I investigated exploits an electrostatic actuation approach to control the mechanical configuration of the SiN membranes. Thanks to the use of an external power supply, it is possible to control the electrostatic force induced between metallic layers deposited around a hole in the membrane and tune the displacement of each point of the membrane with respect to its original position and thus the profile of the hole.

In order to estimate the mechanical response to the applied voltage and optimize the design of the device, I used the finite-element simulation program COMSOL. The software allows creating a 3D model of the device and – using specialized simulation modules for microelectromechanical systems and the correct material properties (dielectric constants, the voltage applied to the device, etc.) – determining the electrostatic response of the system in terms of induced field and charge density configurations. In

the simulation, it is possible to obtain the forces applied to every single surface element of the device and use them as an input to estimate the stress and the deformation profile of the entire structure.

The forces induced by the electrical field were calculated through the Maxwell stress tensor T_{ij} that allows writing the force per unit volume in the form expressed by equation (6.2)

$$T_{ij} = \epsilon_0 (E_i E_j - \frac{1}{2}\delta_{ij} E^2) + \frac{1}{\mu_0}(B_i B_j - \frac{1}{2}\delta_{ij} B^2) \tag{6.1}$$

$$\vec{f} + \epsilon_0 \mu_0 \frac{\partial \vec{S}}{\partial t} = \vec{\nabla} \vec{T} \tag{6.2}$$

where E and B are the electric and magnetic fields and $\vec{S}$ indicates the Poynting vector. The first tested design is depicted in Fig 6.1a: it consists of a SiN membrane with a rectangular hole and two metallic electrodes deposited on its edges, that create a parallel plate capacitor. Since the force applied between the plates increases with the reduction of the width of the hole, a narrow $1\,\mu$m $\times$ $10\,\mu$m rectangle was simulated. After setting one of the plates as the electrical ground and applying a constant voltage to the other one, the resulting forces on the capacitor plates induce a deformation on the SiN membrane. The final displacement, measured on each side of the rectangular hole, is reported in Fig. 6.1b. To cross-check these results, further simulations were made, including "Identity Pair" conditions between the plates of the conductor and the surface of the membrane (i.e. imposing that the two surfaces remain attached during the simulated deformation). As visible from the simulation results, the maximum change in the displacement induced by an applied voltage of 100 V is smaller than 1 nm (the initial displacement different from zero is due to the pre-stress present in the SiN membrane), which implies that the threshold tension necessary to create a useful deformation is too high for practical purposes.

A new and more efficient device design was thus considered and simulated, based on a "comb capacitor" architecture. The device is shown in Fig. 6.1c and includes two sets of intercalated metallic fingers, one connected to the ground and the other to a voltage generator. When voltage is applied to the comb, each finger can slip in the space

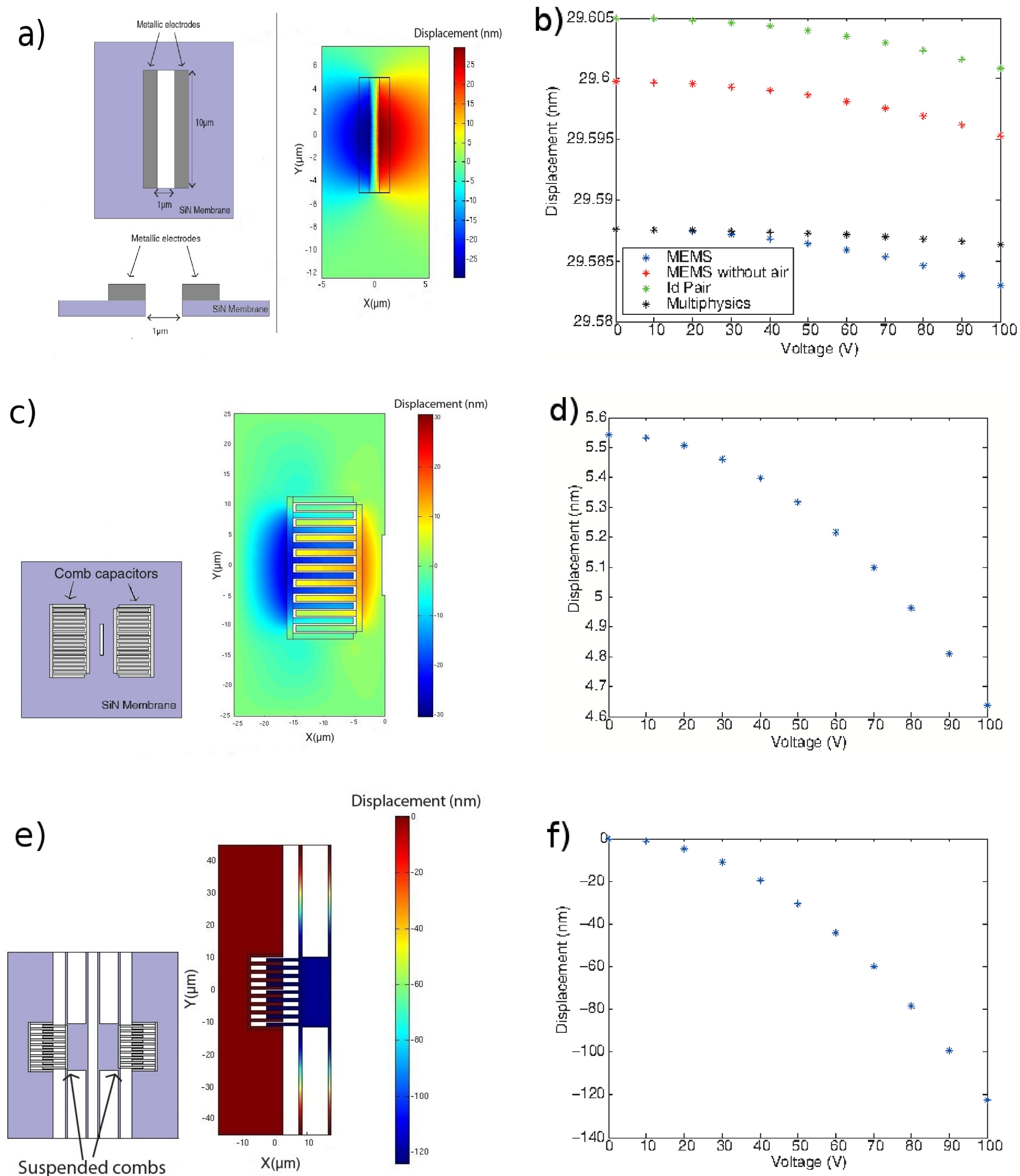

Figure 6.1: Different designs of the device and results of the simulation in relation to the applied tension. Parallel plate capacitor design: simulated displacement induce by (a) an applied voltage of 100V and (b) as a function of the applied tension. Comb capacitor design: simulated displacement induced (c) by an applied voltage of 100V and (d) as a function of the applied tension. Suspended comb capacitor design: simulated displacement induced (e) by an applied voltage of 100V and (f) as a function of the applied tension.

between two neighboring fingers of the opposite set. Since the force induced between the two components of the comb capacitor depends on its geometrical properties, such as the number of fingers and their distance, several initial simulations were run to optimize these parameters and maximize the induced force. The inter-finger distance was chosen to be 0.25 μm with 10 fingers for each comb. The device obtained by placing a comb capacitor on either side of the rectangular hole in the membrane has then been simulated in order to improve the tunability of the device: placing the center of each comb at 10 μm from the center of the membrane, the displacement shown in Fig. 6.1d has been obtained for different voltages applied to the device. Similarly to the parallel plate capacitor case, the voltage required to induce a significant change from the initial configuration of the SiN membrane is still too large for the device to be useful.

A better design for the device to induce strain in graphene using electrostatic forces is shown in Fig. 6.1e: since all the previous architectures required an extremely high voltage to induce a relevant displacement, due to the elastic resistance to deformation opposed by the extensive SiN regions surrounding the slit, the new design was created by attaching the combs on a more flexible piece of SiN suspended by narrow beams playing the role of mechanical springs. After running the simulation to estimate the best geometry to maximize the displacement, I simulated a configuration including a comb suspended on a piece of membrane with 500 nm-wide and 35 μm-long springs and deformation was calculated as a function of the applied voltage. The results shown in Fig. 6.1f demonstrate that the device is much more responsive to the applied tension and allows obtaining a displacement of 100 nm with a drive of 80 V.

These architectures could not be implemented and fabricated as real devices during this thesis project, but test experiments could be performed on a specific MEMS stretcher within a collaboration with the University of Trieste [39].

6.2 MEMS stretcher

A set of test experiments were performed to induce strain in graphene using a MEMS platform designed for the investigation of the impact of strain in living cells, i.e. exploiting a device originally created for biomedical application [39]. The MEMS architecture

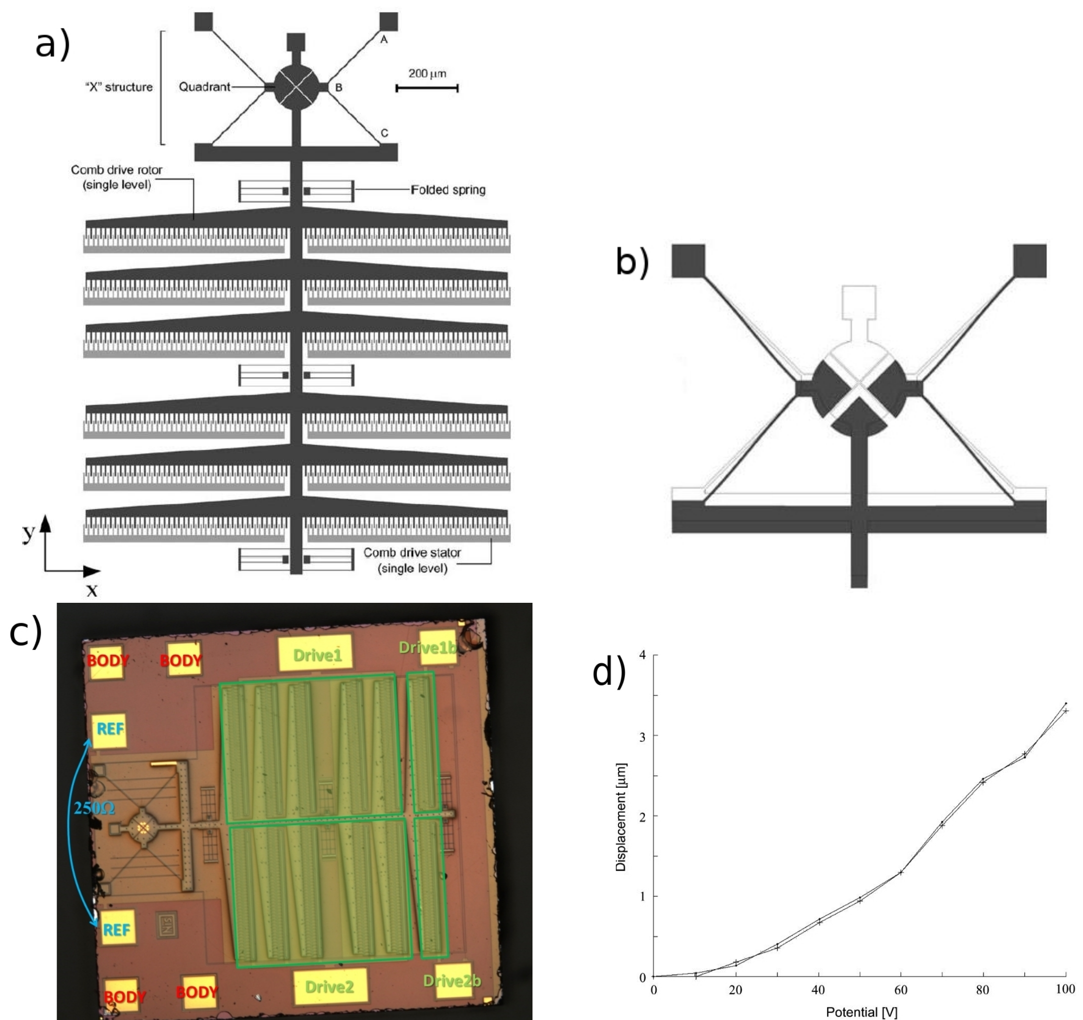

Figure 6.2: MEMS stretcher device [39]. (a) Scheme of its structure and of components. (b) Scheme of the biaxial displacement induced by the comb drive actuator. (c) Optical image of the device and of the connection pads. (d) Generated biaxial displacement as a function of the applied voltage.

is shown in Fig. 6.2a: it consists of a circular plate, sectioned in four quadrants, connected to massive electrostatic driver constituted by 12 set of combs with 42 electrodes each. Folded springs were also added on the device side to provide restoring force and prevent the comb actuator to move sideways.

Voltage is applied to one side of the comb through the pads denominated as "Drive" in the optical picture in Fig. 6.2c, while the rest of the structure is electrically grounded through the "Ref" pads: the pulling force given by the actuator is used to move two of the four quadrant horizontally and the third vertically (see spring arrangement in Fig. 6.2b), thus inducing a biaxial pulling in the circular plate. Two thin beams connect each one of the two lateral section of the central plate to anchoring points of the structure and to the comb drive actuator, reported in Fig. 6.3 as A and C, respectively: due to their angle of 45° and 135° with respect to the horizontal direction and their equal length, any vertical displacement of the point C translates, in a small displacement limit, to a shift of the point B with equal components in both the x and y direction, causing a total shift between opposite quadrants of the circular plate that can be expressed by the equation [39]

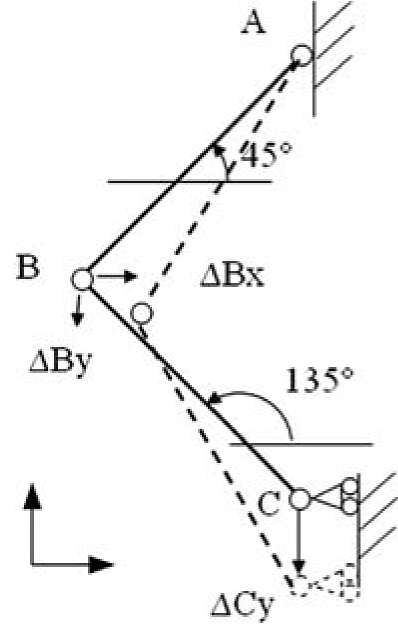

Figure 6.3: Scheme of the mechanism of generation of the biaxial strain. Picture taken from [39].

$$\Delta x = \Delta x_0 + 2\Delta B_x \approx \Delta x_0 + \Delta C_y \tag{6.3}$$

$$\Delta y = \Delta y_0 + 2\Delta B_y = \Delta y_0 + \Delta C_y \tag{6.4}$$

where ΔC_y, ΔB_y and ΔB_x are the displacement of the point B and C in the vertical and horizontal direction and Δx_0 and Δy_0 are the initial distance between opposite quadrants.

Due to the electrostatic nature of the driving force, the displacement of the device is

expected to have a quadratic dependence from the driving voltage. The actual response of the device can be tested by putting the device on a test board under an optical microscope [39]. After the control electrodes are properly wired to a power supply, several images of the circular plate were acquired as a function of the applied voltage. Using an image processing software, it was possible to estimate the distance between the quadrants of the plate: the results of the calibration reported in Ref. [39] are shown in Fig. 6.2d. Similar calibration curves were obtained during the thesis work on the same devices.

The large displacement obtainable with relatively low tension applied makes the device suitable for the graphene strain application. Perliminary work was done to transfer graphene to the top of the MEMS and to clamp it to the circular plate. The MEMS were first of all anchored to the substrate using a drop of PMMA and subsequently freeing the plate region by EBL lithography. Once the plate is cleared from PMMA, the graphene transfer procedure (see paragraph 5.1.2) could be applied without the risk of collapsing the suspended part of the MEMS on the Si bulk substrate. The support PMMA was then removed by immersing the device in acetone and isopropyl alcohol. The sample was finally dried using a critical point dryer (CPD), that allows avoiding problems related to surface tension, which would lead to a collapse of the movable parts of the MEMS on the Si substrate. At the time of the writing of this thesis, anchoring issues prevented to explore by Raman the active deformation of the graphene flakes.

Conclusion

Graphene is a two dimensional material characterized by several interesting properties, making it appealing for different applications in the context of both optoelectronic and opto and electro-mechanics. Among them, the opportunity to tailor its electronic properties through strain is particularly promising and relevant.

Even though recently several different works have focused on the study of strain in graphene and on its consequences, its control is still today a challenging objective. The aim of this thesis has been the creation and the investigation by micro-Raman spectroscopy of different strain configurations on free-standing graphene, obtained by applying a pressure load to a micropatterned SiN membrane with pass-through holes of different sizes and shapes, onto which monolayer graphene has been deposited.

Results obtained from Raman measurements display, for every geometry investigated, an evident redshift of the Raman $2D$ and G peaks in free-standing graphene subjected to a pressure load, indicating a non-zero value of the hydrostatic component of strain. The spatial dependence of the peak intensities has been studied as a function of the hole geometries and dimensions, yielding results in good agreement with the simulation of the strain profiles.

As a novel result, during my thesis I could also demonstrate the presence of an anisotropic component of the strain in the devices with elliptical holes, as proven by the non-trivial evolution of the linewidth of the G peak. A further confirmation of the effect has been obtained thanks to the analysis of the relation between the maximum strain, localized in the center of the free standing area, and the pressure load ΔP applied to the membrane: results, in fact, show a clear splitting of the G peak into its G^+ and G^-

components.

Starting from the same measurements, it has been possible to demonstrate that the dependence of the position of the peaks is linear in $\Delta P^{2/3}$ [38] and thus the strain induced in the suspended graphene can be controlled by the applied differential pressure. The dependence of the peak shift from the pressure load, along with the numerical estimates of the strain, has been used to analyze the experimental evolution of the position of the Raman peaks as a function of the pressure: results have been found to be compatible with those reported in recent works on suspended graphene [12, 13]. In addition, the values of the Grüneisen parameters for the G and $2D$ peaks and of the shear deformation potential for the G peak have been estimated for every geometry of the device, yielding results in good agreement with those reported in the literature [12–14].

In conclusion, the experimental approach here described indicates a new strategy for the creation of arbitrary strain profiles, which can be controlled by the applied pressure and by the geometry of the supporting SiN membrane.

Appendix

Machine	Description
Spin Coater	A spin coater, usually referred to as spinner, is a machine that allows the uniform deposition of thin films on flat substates. It consists of a vacuum chunck, mounted on a rotating support, onto which the sample is placed and locked. After pouring an adequate amount of the chosen substance on the sample with a pipette and closing the lid, the centrifugal force of the rotation together with the surface tension of the substance allows its uniform distribution over the sample. The thickness of the resulting film can be controlled changing parameters as the rotation speed and the acceleration.
Mask Aligner	A mask aligner is a machine used to perform photolithography on samples covered with a thin layer of photoresist. It consists of a mobile stage, moved with micrometric screws in both the xy plane and z direction, that is used to align the sample with the pattern printed on a photomask, which is an opaque plate with trasparent areas placed so to form a precise pattern. The photomask is attached through a vacuum system to a support secured with screws above the mobile stage. The vacuum seal is necessary to prevent any possible scratch on the photomask due to any other blocking system. The alignment between the sample and the pattern on the mask can be checked through an optical microscope positioned above it. Once the sample has been aligned and brought in contact with the mask, it is possible to select the time of exposure and the power of the lamp and expose the sample to the UV light. The process allows to modify the composition of the exposed photoresist,

	making it soluble (positive photoresist) or insoluble (negative photoresist) in its developer.
Reactive Ion Etching	A RIE is a machine that allows etching, i.e. removing the sample's material from its surface, using reactive ions. It typically consists of a vacuum chamber containing two electrodes, used as plates of a capacitor: one at the top of the chamber and one on the bottom, electrically isolated, onto which the sample is placed. Once the chamber is closed and evacuated with a turbomolecular pump (down to a pressure of few $10^{-}6$ mbar), it is filled with different types of gas, chosen according to the material to etch, that are then ionized by the electrical field created between the capacitor's plates, by supplying the electrodes with an RF power. The ions and free radicals thus obtained cause the etching mechanism, by inducing a chemical and physical process: they react with atoms on the sample's surface, releasing volatile components, and transfer some of their kinetic energy, due to the presence of the electric field, though a scattering process, providing the atoms on the surface enough energy to be removed. In order to maintain a constant etching rate, gasses are continuously injected in the chamber through inlets in the top of the camber and, at the same time, part of the gas is removed through a pump. To control the etching's characteristics, such as anisotropy, rate, surface roughness, an accurate selections of the process parameters (gasses concentrations, RF power, flow rate) are requested.
EBL	An EBL is a machine used to perform the electron beam lithography, a process that uses a focused electron beam to

scan and draw custom shapes and patterns on surfaces covered in a film sensitive to electrons. The exposure chemically modifies the resist's structure and makes it soluble (positive resist) or insoluble (negative resist) in its developer.

The lithography system consists of a vacuum chamber, where the samples are placed under a column connected to an electron gun, from where the electrons used in the process are extracted. They are generated from a filament through either thermoionic emission or applying a strong electric field, or both. Electrons thus created are then accelerated and focused by electron lenses, using both electric and magnetic fields, and exit the end of the column as a focused beam, impinging on the sample. To avoid the deposition of impurities or the creation of ions that could damage the sample, due to the interaction of the electron beam with gasses, the chamber is maintained in a state of high vacuum.

The sample is first mounted on a specific holder and then loaded in the EBL system using a "fast entry lock", i.e. a small transfer chamber which can be more easily vented and evacuated, while the main EBL chamber remains in vacuum. Once loaded in the EBL chamber, the sample can be moved and rotated to place the area to be exposed right under the electron beam. The EBL control software, besides controlling the stage's position, the process parameters and beam features (focus, aperture, astigmatism), allows to draw directly the patterns to impress on the sample, based on a a CAD file: using either markers already on the surface or other features, for example a sample's edge, to adjust the reference coordinates for the drawing, the focused beam is deflected and used to scan the areas to be exposed. Parameters such as exposure

	dose, i.e. the amount of charge deposited per unit area, and the beam current depend on the characteristics of the resist film.

Table 1: Description and functioning of the machines used in the mircofabrication process (section 5.1.)

Pressure (mbar)	Position of $2D$ peak (cm^{-1})	Position of G peak (cm^{-1})
0	2674.2±0.4	1582.6±0.3
520	2651.2±0.4	1571.8±0.3
600	2647.9±0.4	1570.6±0.3
720	2642.1±0.4	1568.0±0.3
800	2639.2±0.4	1566.9±0.3

(a)

Pressure (mbar)	Position of $2D$ peak (cm^{-1})	Position of G peak (cm^{-1})
0	2673.2±0.2	1581.6±0.2
200	2664.2±0.2	1577.5±0.2
300	2660.1±0.2	1575.9±0.2
500	2653.0±0.2	1572.6±0.2
600	2650.9±0.2	1571.9±0.2
700	2647.3±0.2	1569.9±0.2
800	2644.1±0.2	1568.3±0.2
900	2641.1±0.2	1567.1±0.2

(b)

Pressure (mbar)	Position of $2D$ peak (cm^{-1})	Position of G^+ peak (cm^{-1})	Position of G^- peak (cm^{-1})
0	2673.5±0.4	1582.3±3.6	1582.3±2.1
400	2647.5±0.5	1574.4±1.6	1568.2±4.0
500	2640.4±0.5	1573.0±1.2	1565.1±2.1
720	2622.8±0.5	1566.2±0.8	1557.5±1.2
800	2617.5±0.5	1565.2±0.8	1555.4±1.1
850	2613.5±0.5	1563.5±1.1	1554.2±1.6
900	2610.4±0.5	1562.0±1.2	1552.4±1.6
950	2606.5±0.6	1560.4±0.9	1550.0±2.0
1000	2604.3±0.6	1559.7±0.9	1549.2±1.5

(c)

Table 2: Table of the position of Raman peaks obtained, varying the differential pressure applied to the membrane, for graphene suspended over a circular hole with a diameter of 10 μm (a), an elliptical hole of dimensions 5 μm × 10 μm (b) and an elliptical hole of dimensions 20 μm × 40 μm (c).

Bibliography

[1] A. K. Geim e K. S. Novoselov. "The rise of graphene". In: *Nature Materials* 6 (3 2007). DOI: 10.1038/nmat1849.

[2] N. M. R. Peres. "*Colloquium*. The transport properties of graphene: An introduction". In: *Rev. Mod. Phys.* 82 (3 2010), pp. 2673–2700. DOI: 10.1103/RevModPhys.82.2673.

[3] Z. Jiang, Y. Zhang, Y.-W. Tan, H.L. Stormer e P. Kim. "Quantum Hall effect in graphene". In: *Solid State Communications* 143 (1-2 2007). DOI: 10.1016/j.ssc.2007.02.046.

[4] K. S Novoselov, V. I. Falko, L. Colombo, P. R. Gellert, M. G. Schwab e K. Kim. "A roadmap for graphene". In: *Nature* 490 (7419 ott. 2012). DOI: 10.1038/nature11458.

[5] F. Bonaccorso, Z. Sun, T. Hasan e A. C. Ferrari. "Graphene photonics and optoelectronics". In: *Nature Photonics* 4 (9 2010). DOI: 10.1038/nphoton.2010.186.

[6] Julien Levallois, Andrew L. Walter, Markus Ostler, Aaron Bostwick, Eli Rotenberg, Thomas Seyller, Dirk van der Marel, Alexey B. Kuzmenko e Iris Crassee. "Giant Faraday rotation in single- and multilayer graphene". In: *Nature Physics* 7 (1 2010). DOI: 10.1038/nphys1816.

[7] Vitor M. Pereira e A. H. Castro Neto. "Strain engineering of graphene's electronic structure". In: *Physical Review Letters* 103 (4 lug. 2009). DOI: 10.1103/PhysRevLett.103.046801.

[8] Hang Zhang, Jhao-Wun Huang, Jairo Velasco Jr, Kevin Myhro, Matt Maldonado, David Dung Tran, Zeng Zhao, Fenglin Wang, Yongjin Lee, Gang Liu, Wenzhong Bao e Chun Ning Lau. "Transport in suspended monolayer and bilayer graphene under strain: a new platform for material studies". In: *Carbon* 69 (apr. 2014). DOI: arXiv:1308.1182.

[9] F. Guinea, M. I. Katsnelson e A. K. Geim. "Energy gaps and a zero-field quantum Hall effect in graphene by strain engineering". In: *Nature Physics* 6 (1 2009). DOI: 10.1038/nphys1420.

[10] Mikkel Settnes, Stephen R. Power e Antti-Pekka Jauho. "Pseudomagnetic fields and triaxial strain in graphene". In: *PHYSICAL REVIEW B* 93 (3 2016). DOI: 10.1103/PhysRevB.93.035456.

[11] Takahiro Morimoto, Yasuhiro Hatsugai e Hideo Aoki. "Cyclotron radiation and emission in graphene — a possibility of Landau-level laser". In: *Journal of Physics: Conference Series* 150.2 (2009), p. 022059.

[12] Y. C. Cheng, Z. Y. Zhu, G. S. Huang e U. Schwingenschloegl. "Gruneisen parameter of the G mode of strained monolayer graphene". In: *PHYSICAL REVIEW B* 83.115449 (2011).

[13] T. M. G. Mohiuddin, A. Lombardo, R. R. Nair, A. Bonetti, G. Savini, R. Jalil, N. Bonini, D. M. Basko, C. Galiotis, N. Marzari, K. S. Novoselov, A. K. Geim e A. C. Ferrari. "Uniaxial strain in graphene by Raman spectroscopy: G peak splitting, Grüneisen parameters and sample orientation". In: *PHYSICAL REVIEW B* 79.205433 (2009).

[14] Jakob Zabel, Rahul R. Nair, Anna Ott, Thanasis Georgiou, Andre K. Geim, Kostya S. Novoselov e Cinzia Casiraghi. "Raman spectroscopy of graphene and bilayer under biaxial strain: bubbles and balloons". In: *Nano Lett.* 12.2 (2012), pp. 617–621. DOI: 10.1021/nl203359n.

[15] A. H. Castro Neto, F. Guinea, N. M. R. Peres, K. S. Novoselov e A. K. Geim. "The electronic properties of graphene". In: *Rev. Mod. Phys.* 81 (1 2009), pp. 109–162. DOI: 10.1103/RevModPhys.81.109.

[16] G. Grosso e G. Pastori Parravicini. *Solid State Physics*. Academic Press, 2014.

[17] S. Roddaro, P. Pingue, V. Piazza, V. Pellegrini e F. Beltram. "The Optical Visibility of Graphene:Interference Colors of Ultrathin Graphite on SiO2". In: *Nano Letters* 7 (9 2007). DOI: 10.1021/nl071158l.

[18] P. Blake, E. W. Hill, A. H. Castro Neto, K. S. Novoselov, D. Jiang, R. Yang, T. J. Booth e A. K. Geim. "Making graphene visible". In: *Applied Physics Letters* 91 (6 2007). DOI: 10.1063/1.2768624.

[19] V. Miseikis, D. Convertino, N. Mishra, M. Gemmi, T. Mashoff, S. Heun, N. Haghighian, F. Bisio, M. Canepa, V. Piazza e C. Coletti. "Rapid CVD growth of millimetre-sized single crystal graphene using a cold-wall reactor". In: *2D Materials* 2.1 (2015), p. 014006.

[20] R.P. Feynman, R.B.Leighton e M. Sands. *The Feynman Lectures on Physics Vol.2*. Addison-Wesley, 1964.

[21] S. Sasic e Y. Ozaki. *Raman, infrared, and near-infrared chemical imaging*. Wiley, 2010.

[22] YuMeng You, ZhenHua Ni, Ting Yu e ZeXiang Shen. "Edge chirality determination of graphene by Raman spectroscopy". In: *Applied Physics Letters* 93 (16 2008). DOI: 10.1063/1.3005599.

[23] Ken ichi Sasaki, Riichiro Saito, Katsunori Wakabayashi e Toshiaki Enoki. "Identifying the orientation of edge of graphene using G band Raman spectra". In: *Journal of the Physical Society of Japan* 79 (4 2010). DOI: 10.1143/jpsj.79.044603.

[24] Chunxiao Cong, Ting Yu e Haomin Wang. "Raman study on the G mode of graphene for determination of edge orientation". In: *ACS Nano* 4 (6 giu. 2010). DOI: 10.1021/nn100705n.

[25] Andrea C. Ferrari e Denis M. Basko. "Raman spectroscopy as a versatile tool for studying the properties of graphene". In: *Nature Nanotechnology* 8 (4 apr. 2013). DOI: 10.1038/nnano.2013.46.

[26] A. C. Ferrari, J. C. Meyer, V. Scardaci, C. Casiraghi, M. Lazzeri, F. Mauri, S. Piscanec, D. Jiang, K. S. Novoselov e S. Roth. “Raman spectrum of graphene and graphene layers”. In: *Physical Review Letters* 97 (18 2006). DOI: 10.1103/physrevlett.97.187401.

[27] L.M. Malard, M.A. Pimenta, G. Dresselhaus e M.S. Dresselhaus. “Raman spectroscopy in graphene”. In: *Physics Reports* 473 (2009), pp. 51–87.

[28] Mingyuan Huang, Hugen Yan, Changyao Chen, Daohua Song, Tony F. Heinz, e James Hone. “Phonon softening and crystallographic orientation of strained graphene studied by Raman spectroscopy”. In: *PNAS* 106.18 (2009).

[29] Ioannis Polyzos, Massimiliano Bianchi, Laura Rizzi, Emmanuel Koukaras, John Parthenios, Konstantinos Papagelis, Roman Sordan e Costas Galiotis. “Suspended monolayer graphene under true uniaxial deformation”. In: *Nanoscale* 7 (30 2015).

[30] C. Thomsen, S. Reich e P. Ordejon. “Ab initio determination of the phonon deformation potentials of graphene”. In: *PHYSICAL REVIEW B* 65.073403 (2002).

[31] Vitor M. Pereira, A. H. Castro Neto e N. M. R. Peres. “Tight-binding approach to uniaxial strain in graphene”. In: *Physical Review B* 80 (4 lug. 2009). DOI: 10.1103/PhysRevB.80.045401.

[32] C. Neumann, S. Reichardt, P. Venezuela, M. Drögeler, L. Banszerus, M. Schmitz, K. Watanabe, T. Taniguchi, F. Mauri, B. Beschoten, S. V. Rotkin e C. Stampfer. “Raman spectroscopy as probe of nanometre-scale strain variations in graphene”. In: *Nature Communications* 6 (set. 2015). DOI: 10.1038/ncomms9429.

[33] Jae-Ung Lee, Duhee Yoon e Hyeonsik Cheong. “Estimation of Young’s modulus of graphene by raman spectroscopy”. In: *Nano Letters* 12 (9 set. 2012). DOI: 10.1021/nl301073q.

[34] J. Maultzsch, S. Reich e C. Thomsen. “Double-resonant Raman scattering in graphite: interference effects, selection rules, and phonon dispersion”. In: *Physical Review B* 70 (15 ott. 2004). DOI: 10.1103/PhysRevB.70.155403.

[35] Pedro Venezuela, Michele Lazzeri e Francesco Mauri. “Theory of double-resonant Raman spectra in graphene: intensity and line shape of defect-induced and two-phonon bands”. In: *Physical Review B* 84 (3 lug. 2011). DOI: 10.1103/PhysRevB.84.035433.

[36] F. Cerdeira, J. C. Buchenauer, Fred H. Pollak e Manuel Cardona. “Stress-Induced Shifts of First-Order Raman Frequencies of Diamond- and Zinc-Blende-Type Semiconductors”. In: *Phys. Rev. B* 5 (2 1972), pp. 580–593. DOI: 10.1103/PhysRevB.5.580.

[37] Changgu Lee, Xiaoding Wei1, Jeffrey W. Kysar e James Hone. “Measurement of the Elastic Properties and Intrinsic Strength of Monolayer Graphene”. In: *Science* 321 (5887 lug. 2008). DOI: 10.1021/nl301073q.

[38] Yuyoung Shin, Marcelo Lozada-Hidalgo, Jose L. Sambricio, Irina V. Grigorieva, Andre K. Geim e Cinzia Casiraghi. “Raman spectroscopy of highly pressurized graphene membranes”. In: *Applied Physics Letters* 108.22 (2016), p. 221907. DOI: 10.1063/1.4952972.

[39] N. Scuor, P. Gallina, H. V. Panchawagh, R. L. Mahajan, O. Sbaizero e V. Sergo. “Design of a novel MEMS platform for the biaxial stimulation of living cells”. In: *Biomed Microdevices* 8 (2006), pp. 239–246. DOI: 10.1007/s10544-006-8268-3.